2019

Magnetic Domain Structures in Fe-Ga Alloys

Matthew N. Tianen
Michigan Technological University, mntianen@mtu.edu

MAGNETIC DOMAIN STRUCTURES IN FE-GA ALLOYS

By

Matthew N. Tianen

A DISSERTATION

Submitted in partial fulfillment of the requirements for the degree of

DOCTOR OF PHILOSOPHY

In Materials Science and Engineering

MICHIGAN TECHNOLOGICAL UNIVERSITY

2019

This dissertation has been approved in partial fulfillment of the requirements for the Degree of DOCTOR OF PHILOSOPHY in Materials Science and Engineering.

Department of Materials Science and Engineering

Dissertation Advisor:	*Yongmei Jin*
Committee Member:	*Stephen Hackney*
Committee Member:	*Keat Ong*
Committee Member:	*Aleksey Smirnov*
Department Chair:	*Stephen Kampe*

Table of Contents

Acknowledgements

Support from NSF DMR-1409317 is acknowledged.

Special thanks are given to Dr. Keat Ong and Salil Karipott for their invaluable assistance developing instrumentation for this work, and to Dr. Yongmei Jin for her consistent and patient guidance.

Abstract

Fe-Ga alloys, also referred to as Galfenol, have attracted great attention as new giant magnetostrictive materials for over fifteen years. They exhibit large magnetostriction, small hysteresis, good machinability, and high tensile strength, providing many advantages over other functional materials like magnetostrictive Terfenol-D, piezoelectric PZT, and magnetic shape memory Ni-Mn-Ga. In spite of the intense interest in Fe-Ga alloys, the domain phenomena that underlie their properties and functionalities are less known. Using the Bitter method, a systematic study of magnetic domain structures in Fe-Ga single crystals of different compositions and heat treatments has been performed. Our domain observation experiments reveal numerous previously unknown domain patterns and their responses to magnetic fields. Zigzag domain walls, previously observed in Galfenol, are reinterpreted as V-lines formed by the meeting of two domain walls. Two types of charged 90° domain walls are described for the first time in this material, including a new type of zigzag wall.

As a cubic system of high magnetostriction and weak magnetocrystalline anisotropy, the domains on Fe-Ga surfaces are largely determined by the image forces (both magnetostatic and elastostatic) associated with the surfaces, making it challenging to infer inner bulk domains from surface observations, while the bulk domains dominate the material responses. Using domain theory, the observed domain structures and their evolutions near the surfaces were analyzed. The findings advance our understanding of the domain phenomena and mechanisms responsible for the magnetoelastic behaviors of Fe-Ga alloys.

1 Introduction and Background

1.1 Introduction

Fe-Ga alloys, also known as galfenol, show great promise as magnetostrictive materials. Magnetistriction up to ~400 ppm has been demonstrated at certain compositions [1]. It also has good strength and ductility compared to the more brittle magnetostrictive Terfenol-D and piezoelectric PZT (lead zirconate titanate). For example, single crystal $Fe_{83}Ga_{17}$ had a tensile strength of 580 MPa, yield strength of 450 MPa, and elongation of 1.6% on a [110] tensile axis and a yield strength of 515 MPa and 2% elongation on a [100] tensile axis [2]. Polycrystalline $Fe_{81.6}Ga_{18.4}$ with a [100] preferred orientation had a tensile strength of 370 MPa and a 1.2% elongation [3]. The relatively high ductility means galfenol is more machineable than its brittle counterparts. Due to its attractive properties, galfenol has seen use in a wide range of applications, including linear actuators [4, 5], bimetal bending actuators [6-8], vibration generation [9], and energy harvesting [10]. While it has many advantages, not much is known about the mechanisms driving the behavior of this material. The reason for the large magnetostriction is not fully understood and the magnetic domain structure has not been thoroughly characterized.

This work seeks to address the lack of knowledge about magnetic domains in galfenol. The bulk of magnetic domain characterization has revolved around false domain structures resulting from poor surface preparation. Recent work by Chopra and Wuttig [11] revealed a new "cellular" domain structure, which is still poorly understood. Here, new interpretations will be explored for this cellular structure. Entirely new domain structures will also be presented, which have never been demonstrated in galfenol before.

1.2 Magnetic Properties of Galfenol

A short summary of magnetic properties of galfenol is included here for context. Galfenol is a soft magnetic material with very low hysteresis and effectively no coercivity. It has cubic anisotropy with <100> easy directions. Values of the anisotropy constants, K_1

and K_2, are shown in Table 1.1, collected by Rafique et al. from single crystals in the as-grown state [12]. A discussion of magnetic anisotropy is given in Section 1.3.2.

Composition (at% Ga)	K_1 (KJ/m^3)	K_2 (KJ/m^3)
5	66	-135
12.5	49	-110
14	46	-96
18	33	-79
20	-2	14

Table 1.1: Anisotropy constants, K_1 and K_2 for different compositions of galfenol.

Values of saturation magnetization for a few compositions are shown in Table 1.2, collected by Restorff et al. using polycrystals in the as grown state [13].

Composition (at% Ga)	Saturation Magnetization, $\mu_0 M_s$ (T)
12.5	1.74
18.4	1.62
18.4	1.61
18.4	1.58
19.5	1.53
22	1.36

Table 1.2: Values of saturation magnetization for different compositions of galfenol.

A few values of the magnetostriction constants λ_{100} and λ_{111} are given in Table 1.3, collected by Clark et al. from as-grown single crystals. For a wider range of values of λ_{100} for quenched and as-grown samples, refer to Figure 1.14. Magnetostriction will be discussed in Section 1.3.4.

Composition (at% Ga)	λ_{100} (ppm)	λ_{111} (ppm)
5.8	79	
13.2	210	
17	311	
18.7	395	
24.1	270	
27.2	350	
8.6		-27
13.2		-24
20.88		42
28.63		61

Table 1.3: Magnetostriction constants λ_{100} and λ_{111} for different compositions of galfenol.

1.3 Basics of Magnetism

Before exploring the complex magnetic domain behavior of galfenol alloys, it is helpful to understand the energetics of ferromagnetic materials and the fundamentals of magnetic domain theory.

1.3.1 Exchange Energy

Ferromagnetism arises as result of the exchange interaction. The exchange interaction is a quantum effect which tends to align magnetic moments parallel to each other. Large scale magnetized bodies are made possible by the alignment caused by the exchange interaction. As long as the exchange effect is stronger that thermal effects, this ferromagnetic state will dominate. The form of the exchange energy is given by Eq. 1.

Eq. 1 $$E_x = A \int |\nabla m|^2 dV$$

The value A is the exchange constant, a material constant, and m is the direction of the magnetization. Exchange energy is a gradient effect that resists changes in the magnetization direction. It is a short-range interaction, and its effects are seen most clearly inside of domain walls.

1.3.2 Magnetic Anisotropy

The energy associated with a magnetization state is also related to orientation with respect to the crystal lattice. This anisotropy energy dictates which magnetization orientations are allowed in the material. The orientations of lowest energy are called "easy directions," and in general the magnetization will occur along these easy directions. For a cubic material, the anisotropy energy per unit volume is given by Eq. 2.

Eq. 2 $$e_K = K_1(m_1^2m_2^2 + m_1^2m_3^2 + m_2^2m_3^2) + K_2m_1^2m_2^2m_3^2$$

The constants K_1 and K_2 are the first and second order anisotropy constants which are unique to each material. The components m_1, m_2, and m_3 are components of the magnetization direction parallel to [100], [010] and [001] respectively. The magnitudes and signs of K_1 and K_2 dictate which directions are easy directions. By minimizing the energy in Eq. 2, it is possible to find which values of K will correspond to the three possible easy directions: <100>, <110>, and <111>. Using Eq. 3 as a condition, the ranges of K for each easy direction can be found through the method of Lagrange multipliers.

Eq. 3 $$m_1^2 + m_2^2 + m_3^2 = 1$$

This is done by finding the stationary points in Eq. 4, where λ is the Lagrange multiplier.

Eq. 4 $$e_K = K_1(m_1^2m_2^2 + m_1^2m_3^2 + m_2^2m_3^2) + K_2m_1^2m_2^2m_3^2 \\ -\lambda(m_1^2 + m_2^2 + m_3^2 - 1)$$

The first step is finding the partial derivatives of e_K with respect to m_1, m_2, and m_3. For m_1 this is shown in Eq. 5, simplified in Eq. 6.

Eq. 5 $$\frac{\partial e_K}{\partial m_1} = K_1(2m_1m_2^2 + 2m_1m_3^2) + 2K_2m_1m_2^2m_3^2 - 2m_1\lambda = 0$$

Eq. 6 $$\frac{\partial e_K}{\partial m_1} = 2m_1[K_1(m_2^2 + m_3^2) + K_2m_2^2m_3^2 - \lambda] = 0$$

The same can be done for m_2 and m_3.

Eq. 7 $$\frac{\partial e_K}{\partial m_2} = 2m_2[K_1(m_1^2 + m_3^2) + K_2m_1^2m_3^2 - \lambda] = 0$$

Eq. 8 $$\frac{\partial e_K}{\partial m_3} = 2m_3[K_1(m_1^2 + m_2^2) + K_2m_1^2m_2^2 - \lambda] = 0$$

It is helpful to first consider some simplified cases. The first case is $K_1=0$. If $K_1=0$ then Eq. 2 reduces to Eq. 9.

Eq. 9 $$e_K = K_2m_1^2m_2^2m_3^2$$

For $K_2>0$, the energy is minimized if any component of m is zero. The easy direction is then form <ab0> for any a and b subject to $a^2+b^2=1$. For this case, <100> and <110> are both easy directions. For $K_2<0$, the largest negative energy value must be found by solving Eq. 6, Eq. 7, and Eq. 8. For $K_1=0$ these are reduced to Eq. 10, where i, j, and k can be 1, 2, or 3 interchangeably.

Eq. 10 $$\frac{\partial e_K}{\partial m_i} = m_i\left[K_2m_j^2m_k^2 - \lambda\right] = 0$$

Since $m_i=0$ would result in an energy of zero, the minimization must follow Eq. 11.

Eq. 11 $$m_j^2 m_k^2 - \lambda = 0$$

Inputting values for j and k and setting the equations equal gives Eq. 12.

Eq. 12 $$m_1^2 m_2^2 = m_2^2 m_3^2 = m_3^2 m_1^2$$

This is satisfied by $m_1^2=m_2^2=m_3^2$, so for $K_1=0$ and $K_2<0$, [111] is the easy direction.
The second case to consider is $K_2=0$. In this case Eq. 2 becomes Eq. 13.

Eq. 13 $$e_K = K_1(m_1^2 m_2^2 + m_1^2 m_3^2 + m_2^2 m_3^2)$$

The energy is reduced to zero if two m components are zero, so for $K_1>0$, the easy direction is [100]. As before, if $K_1<0$, the partial derivatives must be solved. In this case, these reduce to Eq. 14.

Eq. 14 $$\frac{\partial e_K}{\partial m_i} = m_i K_1\left(m_j^2 + m_k^2\right) = 0$$

The case of $m_i=0$ is again discarded resulting in Eq. 15.

Eq. 15 $$m_j^2 + m_k^2 = 0$$

Inserting values for j and k and setting the equations equal gives

Eq. 16 $$m_1^2 + m_2^2 = m_2^2 + m_3^2 = m_3^2 + m_1^2$$

This is satisfied by $m_1^2=m_2^2=m_3^2$, so for $K_2=0$ and $K_2<0$, [111] is the easy direction.
The third case, when $K_1\neq0$ and $K_2\neq0$, is the least simplified. In this case the three possible easy directions are entered in Eq. 2. For [100] the energy is given by Eq. 17.

Eq. 17 $$e_{K100} = 0$$

For [110], m=$[\frac{1}{\sqrt{2}}, \frac{1}{\sqrt{2}}, 0]$ and the energy is given by Eq. 18.

Eq. 18 $$e_{K110} = \frac{1}{4}K_1$$

For [111], m=$[\frac{1}{\sqrt{3}}, \frac{1}{\sqrt{3}}, \frac{1}{\sqrt{3}}]$ and the energy is given by Eq. 19.

Eq. 19 $$e_{K111} = \frac{1}{3}K_1 + \frac{1}{27}K_2$$

By finding where Eq. 17, Eq. 18, and Eq. 19 are equal, the boundary conditions for the different easy directions can be determined. Solving $e_{K100} = e_{K110}$ gives $K_1=0$, solving $e_{K100} = e_{K111}$ gives $K_2=-9K_1$, and solving $e_{K110} = e_{K111}$ gives $K_2=-\frac{9}{4}K_1$. Using these boundary conditions and the boundary conditions from the first two cases Figure 1.1 was constructed. Figure 1.1a shows the dependence of the easy direction on the values of K_1 and K_2. In Figure 1.1b, the "hard" and "medium" directions are shown as well. These are the directions representing the highest energy state and an intermediate energy state, respectively. The energy of these other directions is important to consider in regions like the magnetic domain wall, where the magnetization moves away from the easy direction.

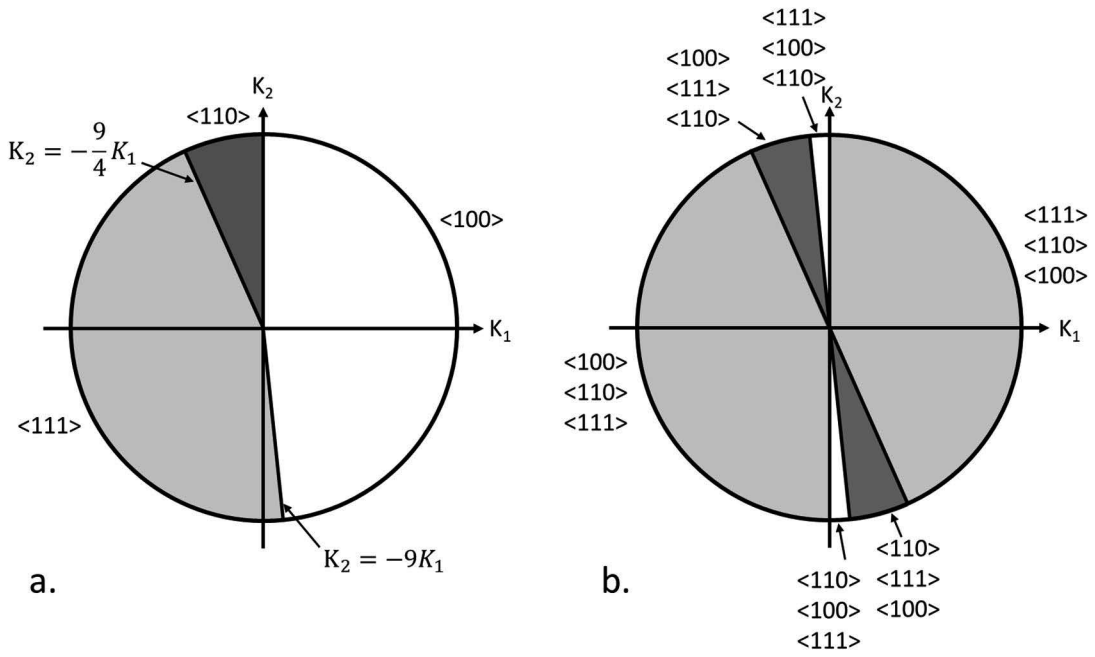

Figure 1.1: Easy and hard directions in a cubic system as a function of K_1 and K_2. The preferred easy directions are plotted as a function of K_1 and K_2 in (a). In (b), the easy, medium, and hard directions are represented. They are shown in ascending order with the lowest energy direction on the bottom and the highest energy on top.

By plotting the energy as a function of direction in spherical coordinates it becomes easier to visualize the easy directions. Figure 1.2 shows spherical plots of e_K+C for different values of K_1 and K_2. The constant C is added to plots of negative anisotropy so that the easy directions always appear as minima. Parts a-c show easy directions of <100>, <110>, and <111> respectively. Parts d-f show the special cases where two easy directions coexist. Figure 1.2d shows the boundary where case K_1=0, part e shows the case $K_2 = -\frac{9}{4}K_1$, and part f shows the case K_2 = -9K_1. For galfenol, the easy direction is <100>. The constants selected for Figure 1.2a are representative of $Fe_{95}Ga_5$ (K_1 = 66 KJ/m^3, K2 = -135 KJ/m^3) [12].

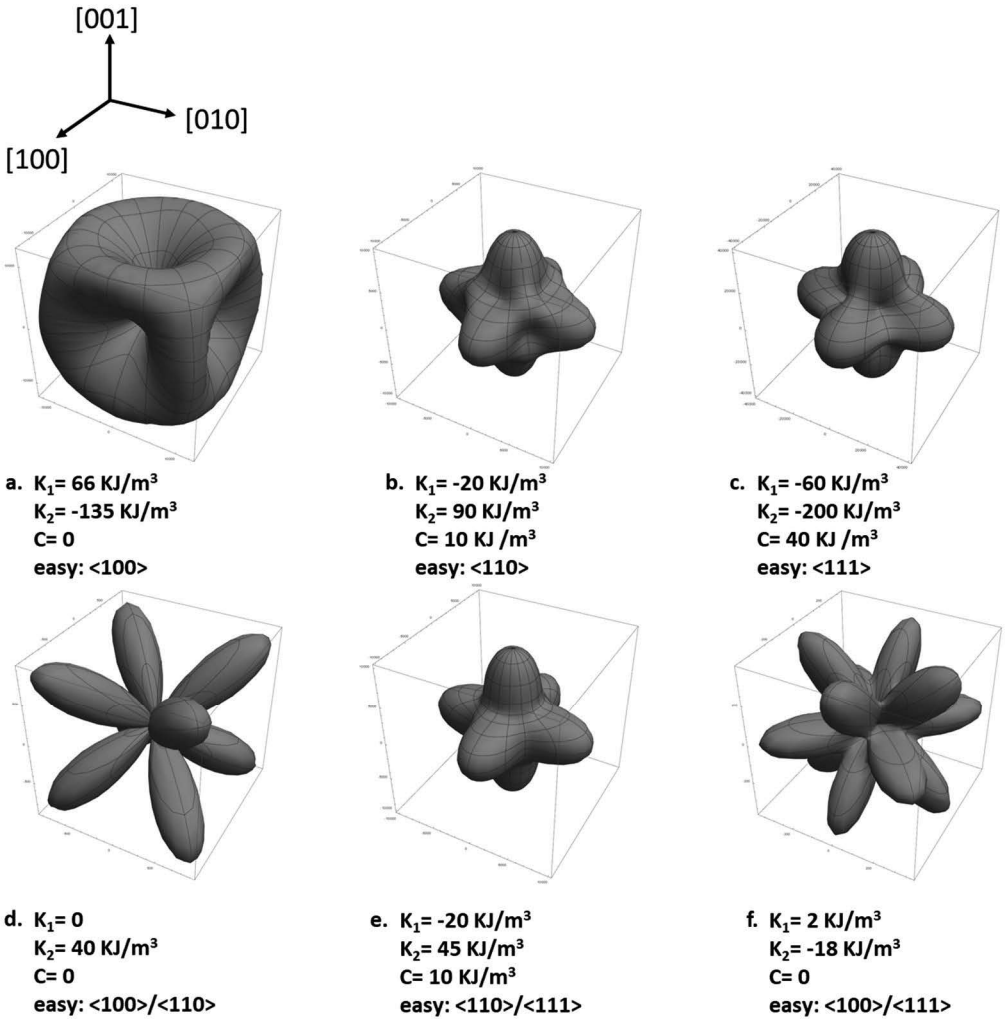

Figure 1.2: Spherical plots of anisotropy energy, e_K, for different values of K_1 and K_2. A constant C was added to e_K for cases with negative anisotropy so that the easy directions consistently appear as minima.

1.3.3 Magnetostatic Energy

While exchange energy and anisotropy are local effects, the magnetostatic energy is a long-range interaction. Magnetostatic energy is the result of the stray field (or demagnetizing fields) and is sometimes also called stray field energy. Stray fields are magnetic fields that result from the discontinuities in the magnetization state of the

material. The stray field, H_d, is defined by the divergence of the magnetization, as in Eq. 20, where M is magnetization.

Eq. 20 $$div\,\overrightarrow{H_d} = -div\,(\vec{M})$$

The stray field energy is then described by Eq. 21, where the integral is taken over the volume of the sample and μ_0 is the permeability of a vaccuum.

Eq. 21 $$-\frac{1}{2}\mu_0 \int \overrightarrow{H_d} \cdot \vec{M} dV$$

The stray field arises from an effective magnetic charge within the material. The volume charge density λ_v and the surface charge density σ_s are defined by Eq. 22 and Eq. 23 respectively.

Eq. 22 $$\lambda_v = -div\,\mu_0 \vec{M}$$

Eq. 23 $$\sigma_s = \mu_0(\overrightarrow{M_1} - \overrightarrow{M_2}) \cdot \vec{n}$$

The vector n is the outward pointing normal direction of a surface separating two regions of different magnetization vectors, M_1 and M_2. The surface could be a free surface, a grain boundary, or a domain wall. For free surfaces or boundaries with a nonmagnetic phase, m_2 is zero. These charge densities are used to define the potential of the stray field, given by Eq. 24 where r and r' are positions in the material.

Eq. 24 $$\Phi_d(\vec{r}) = \frac{1}{4\pi\mu_0}\left[\int \frac{\lambda_v(\vec{r}\prime)}{|\vec{r}-\vec{r}'|} dV' + \int \frac{\sigma_s(\vec{r}\prime)}{|\vec{r}-\vec{r}'|} dS'\right]$$

The magnetostatic or stray field energy, E_d, can then be determined by Eq. 25.

Eq. 25 $$E_d = \frac{1}{2}\left[\int \lambda_v(\vec{r})\Phi_d(\vec{r}) dV + \int \sigma_s(\vec{r})\Phi_d(\vec{r}) dS\right]$$

In general, Eq. 24 and Eq. 25 must be solve numerically, except in some special cases. Some conclusions can be drawn from them though. Since the stray fields act over a long range, magnetically charged surfaces produce a magnetostatic energy in the whole volume of the material. This provides a strong driving force for the elimination of surface charges, and this is the primary driving force for the formation of magnetic domains.

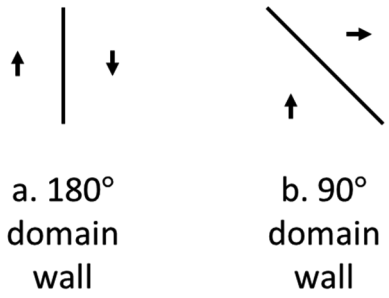

Figure 1.3: Examples of charge free domain walls in a cubic material with <100> easy directions, viewed from a [001] surface. A 180° wall is shown in (a), and a 90° domain wall with Ψ=90° is shown in (b).

Domain structures, whenever possible, will form flux closure patterns which eliminate all surface charges. The types of domain walls that are allowed are dictated by a condition of zero surface charge.

Eq. 26 $$\left(\overrightarrow{M_1} - \overrightarrow{M_2}\right) \cdot \vec{n} = 0$$

Domain walls that meet this condition are considered charge-free. For a cubic material with <100> easy directions there are two possible solutions to this equation. If M_1 and M_2 are both perpendicular to n and oppose each other, the result is a 180° domain wall, so called because the magnetization changes by 180° across the wall. The other possibility is a 90° domain wall where the magnetization changes by 90°. Examples of the two domain wall types are shown in Figure 1.3. There are a range of orientations of the 90° wall that are uncharged. This is demonstrated in Figure 1.4. The wall can rotate along the angle Ψ and always satisfy Eq. 26. In practice, the orientations of the 90° domain wall are constrained by another consideration: the magnetoelastic energy.

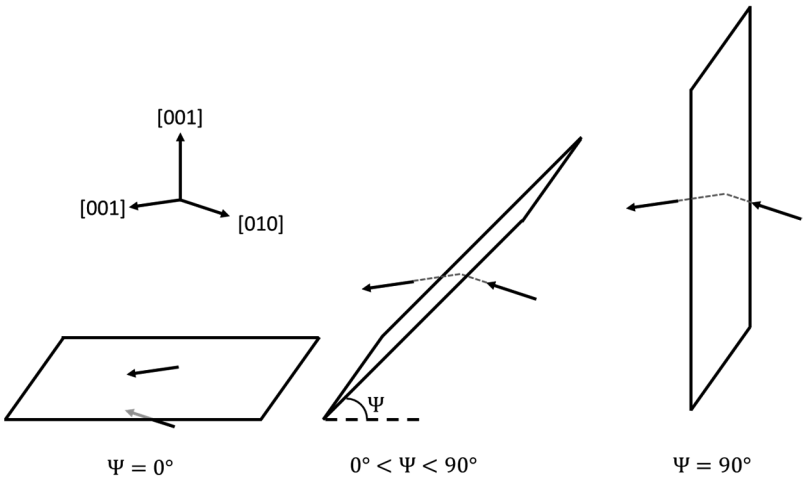

Figure 1.4: Possible charge-free orientations of 90° domain walls. The wall can rotate at any value of the angle Ψ.

1.3.4 Magnetoelastic Energy

Another important term to consider is magnetoelastic energy, the energy arising from magnetostriction. Magnetostriction is a strain induced by the magnetization of the material. Eq. 27 defines the saturation magnetostriction, λ_s, the magnetostrictive strain at saturation relative to a demagnetized state.

Eq. 27 $$\lambda_s = \frac{3}{2}\lambda_{100}\left(m_1^4 + m_2^4 + m_3^4 - \frac{1}{3}\right) + 3\lambda_{111}(m_1^2 m_2^2 + m_2^2 m_3^2 + m_3^2 m_1^2)$$

The material constants λ_{100} and λ_{111} represent the saturation magnetostriction in the [100] and [111] directions respectively, and m_1, m_2, and m_3 are components of the magnetization direction. Eq. 27 only applies when determining the magnetostriction in the direction of the magnetization. To find the magnetostriction in any arbitrary direction, defined by the components b_1, b_2, and b_3, Eq. 28 is used.

Eq. 28 $$\lambda_s = \frac{3}{2}\lambda_{100}\left(m_1^2 b_1^2 + m_2^2 b_2^2 + m_3^2 b_3^2 - \frac{1}{3}\right)$$
$$+3\lambda_{111}(m_1 m_2 b_1\, b_2 + m_2 m_3 b_2 b_3 + m_3 m_1 b_3 b_1)$$

The general strain state is represented by a second rank tensor, ε_{ij}.

Eq. 29
$$\varepsilon_{ij} = \begin{cases} \frac{3}{2}\lambda_{100}\left(m_i^2 - \frac{1}{3}\right), & i = j \\ \frac{3}{2}\lambda_{111} m_i m_k, & i \neq j \end{cases}$$

The magnetostrictive strain state can help to explain why not all 90° walls have equal energy. Domain walls which are elastically compatible (i.e. those without any misfit strain) are preferred. The misfit strain, $\Delta\varepsilon$, is defined as the difference between the strain states $\varepsilon^{(1)}$ and $\varepsilon^{(2)}$ in two adjacent domains.

Eq. 30
$$\Delta\varepsilon = \varepsilon^{(1)} - \varepsilon^{(2)}$$

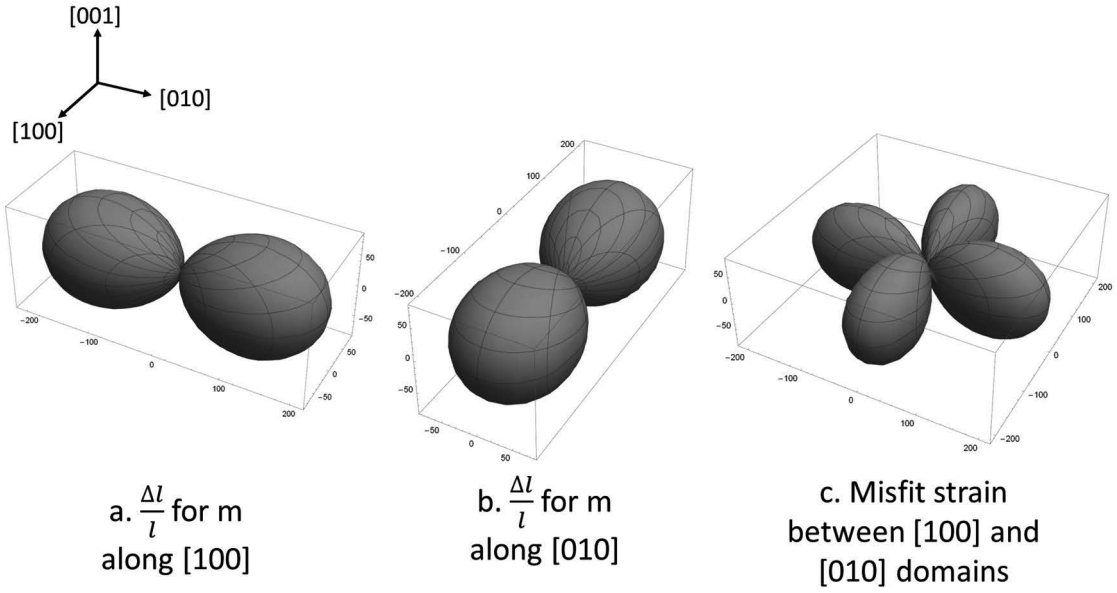

Figure 1.5: Misfit strain on 90° domain walls in $Fe_{86.8}Ga_{13.2}$. Plots of magnetostrictive strain (in ppm) are given for magnetization along [100] (a) and [010] (b). The absolute value of the misfit strain is shown in (c).

Figure 1.5 shows a spherical plot of the magnetsostrictive strain for $Fe_{86.8}Ga_{13.2}$ [1] magnetized in the [100] and [010] directions, as well as the absolute value of the misfit strain. For a domain wall to be compatible, the plane of the wall must pass through a zero-

strain region of Figure 1.5c. This is only possible for the (110) and $(\bar{1}10)$ planes. Since the $(\bar{1}10)$ plane is not stray field free, this leaves only the (110) domain wall.

To explore this idea further, the misfit strain for a 90° domain wall is plotted as a function of the angle Ψ. Figure 1.6 is a polar plot of the absolute value of the misfit strain on the plane of the domain wall. At Ψ = 90° there is no misfit strain. The mistfit strain increases continuously as the angle Ψ decreases from 90° to 0°. Assuming the anisotropy energy and exchange energy are equivalent throughout the wall thickness for any value of Ψ, the orientation will be chosen to minimize the elastic energy resulting from misfit strain. This is the classical view, with 90° domain walls always occurring on the (110)-type planes at 45° to the magnetization direction in a head-to-tail orientation. However, as will be discussed later for zigzag folding of 90° walls, the classical treatment is incorrect, and domain walls with values of Ψ other than 90° do occur.

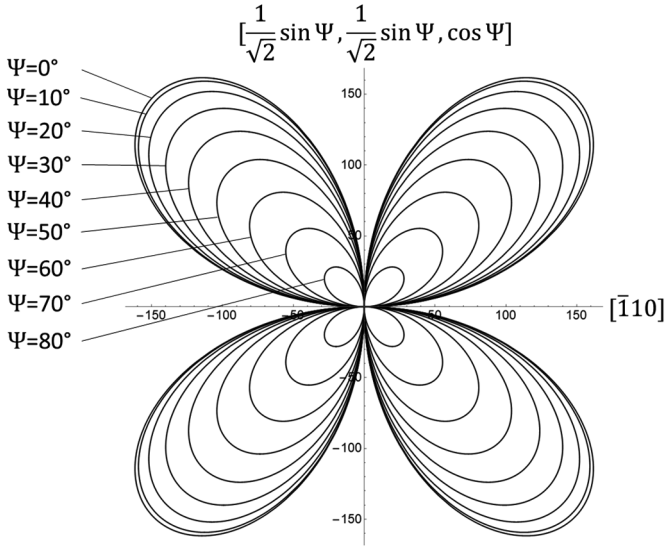

Figure 1.6: Plot of the absolute value of the misfit strain (in ppm) on a 90° domain wall in $Fe_{86.8}Ga_{13.2}$ for different wall angles, Ψ. The horizontal axis is always in the $[\bar{1}10]$ direction, but the orientation of the vertical axis depends on Ψ.

The strain misfit approach is a crude first approximation, but good enough to describe the general behavior in 90° domain walls. In reality, the magnetoelastic energy represents a long-range effect like the magnetostatic energy. If a domain wall has a nonzero

misfit strain, the elastic incompatibility generates stresses even at long distances from the wall. In general, the magnetoelastic energy is orders of magnitude weaker than the magnetostatic energy. However, its effects are more significant in so-called giant magnetostrictive materials, like galfenol. Also, since it is a long-range volume effect, its influence cannot always be disregarded.

The mathematical description of the magnetoelastic energy is quite complex. Eq. 31 gives a general expression for the magnetoelastic energy, E_{el}, in the absence of an applied stress [14, 15].

Eq. 31
$$E_{el} = \frac{1}{2}\int C_{ijkl}\,\varepsilon^0_{ij}(r)\varepsilon^0_{kl}(r)d^3r - \frac{1}{2V}C_{ijkl}\int \varepsilon^0_{ij}(r)\,d^3r \int \varepsilon^0_{ij}(r')\,d^3r'$$

$$-\frac{1}{2}\int \frac{d^3k}{(2\pi)^3} e_i\,\Delta\tilde{\sigma}_{ij}{}^0(k)\Omega_{jk}(e)\Delta\tilde{\sigma}_{kl}{}^0(k)^* e_l$$

In this formulation C_{ijkl} is a fourth rank tensor representing the elastic moduli, ε^0_{ij} is a second rank tensor representing the spontaneous strain from magnetostriction, r is a real space position, k is a reciprocal space position, e_i is a unit vector direction $k_i/|k|$ in reciprocal space, $\tilde{\sigma}^0_{ij}$ is the Fourier transform of $C_{ijkl}\varepsilon^0_{ij}$, and Ω_{ij} is the Green function tensor inverse of the tensor $G_{ik}^{-1}(k) = C_{ijkl}k_jk_l$. This expression must be solved numerically, and minimizing it is not a trivial task. It does, however, demonstrate the non-local quality of the magnetoelastic energy.

The full form of the magnetoelastic energy will not be used in this work. Whenever possible, magnetoelastic effects will be considered qualitatively in terms of how they interact with other energy terms. Any quantitative approaches will be cursory and simplified, like the misfit strain on the 90° domain wall. As will be discussed later, the misfit strain is not the only contribution to the elastic energy. This idea will be explored in greater detail in the discussion of chain domain structures.

1.3.5 External Magnetic and Elastic Energy

The final energy terms to consider are the energy created by external magnetic fields and external stresses. Energy from external magnetic fields is generally referred to as Zeeman energy, which takes the form of Eq. 32.

Eq. 32 $$E_H = -\mu_0 \int \vec{H}_{ex} \cdot \vec{M}\, dV$$

The Zeeman energy is lowest when the external field, H_{ex}, is aligned with the magnetization.

The external elastic energy, $E_{el\text{-}ext}$, is given by Eq. 33, where σ_{ij}^{appl} is a second rank tensor representing the applied stress.

Eq. 33 $$E_{el-ext} = -\sigma_{ij}^{appl} \int \varepsilon_{ij}^{0}(r) d^3 r$$

This energy is lowest when magnetic domains are aligned with tensile stresses.Consider the four domains in Figure 1.7. If a magnetic field is applied from left to right, domain 4 has the lowest energy, domain 2 has the highest energy, and domains 1 and 3 have intermediate energies. In this field domain 4 would grow at the expense of the others.

For a compressive stress applied along the horizontal direction, domains 1 and 3 would have the lowest energy and domains 2 and 4 the highest energy. This is because the magnetostrictive strains in domains 1 and 3 are compressive in the horizontal direction, so they are more compatible with the applied stress. For a tensile stress the opposite behavior would be observed.

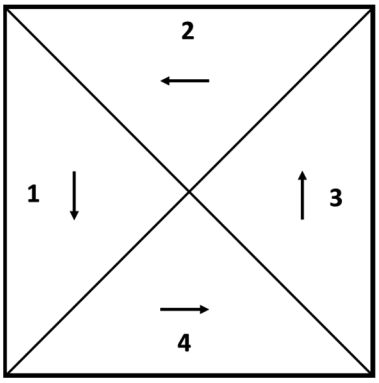

Figure 1.7: Response of magnetic domains to applied fields and stresses. For a magnetic field applied from left to right, domain 4 has the lowest energy and domain 2 has the highest energy. Domain 4 will grow at the expense of the others. If a compressive stress is applied on the horizontal direction, domains 1 and 3 have the lowest energy and grow at the expense of domains 1 and 3.

1.3.6 Bloch Walls

The simplest case of a domain wall is a 180° Bloch wall. In a Bloch wall the magnetization remains parallel to the domain wall while rotating from one domain to the other. This rotation mode results in zero divergence of the magnetization and a stray field free wall. This would be expected in the bulk of a material, far from any surfaces. Stray field effects at the surface can cause deviations from this behavior. The theoretical description of Bloch walls was first developed by Landau and Lifshitz [16]. They described the energy and magnetization distribution for a material of uniaxial anisotropy, having one easy axis of magnetization (e.g. hexagonal cobalt). This is the simplest case and the version of the derivation which will be discussed here. This concept will be expanded upon later when discussing more complex domain structures. The version of the derivation used here follows Hubert and Schafer [17], but is expanded to include more details.

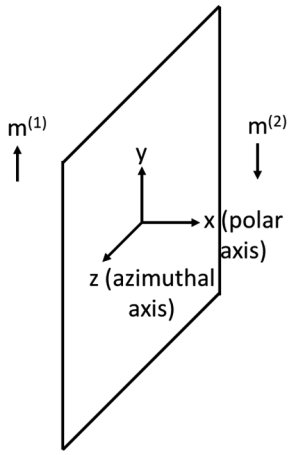

Figure 1.8: Coordinate system for 180° Bloch wall. The domains are magnetized along the y-axis with a domain wall normal to the x-axis. For derivations in spherical coordinates x is the polar axis and z is the azimuthal axis. The polar angle is θ and the azimuthal angle is φ.

To begin, consider a single domain wall in an infinite material, separating two domains of opposite magnetization. The x-axis lies normal to the surface of the wall. The two domains are magnetized along the positive and negative y-axis. The z-axis, which also lies in the plane of the wall, represents the hard direction. The magnetization rotates continuously from positive y to negative y, remaining parallel to the wall. This path is expected because it is the shortest path and is stray field free. The coordinate system is summarized in Figure 1.8. The magnetization angle is referenced in spherical coordinates. The polar axis and angle are x and θ respectively and the azimuthal axis and angle are y and φ respectively.

For a material of uniaxial anisotropy, the anisotropy energy is given (to first order) by Eq. 34 where θ_u is the angle between the magnetization and the easy axis.

Eq. 34 $$e_K = K_{u1} \sin^2 \theta_u$$

With the azimuthal axis as the hard axis, this can be rewritten in terms of φ.

Eq. 35 $$e_K = K_{u1} \cos^2 \varphi$$

Since the magnetization only changes with respect to x, the exchange energy in Eq. 1 reduces to

Eq. 36 $$E_x = A\int_{-\infty}^{\infty} \varphi'^2 dx$$

The quantity φ' is a derivative with respect to x. If the anisotropy energy is also integrated over all x, Eq. 35 and Eq. 36 can be combined to form an expression for the Bloch wall energy, γ_w.

Eq. 37 $$\gamma_w = \int_{-\infty}^{\infty} [A\varphi'^2 + K_{u1}\cos^2\varphi] dx$$

The boundary conditions are as follows: $\varphi(-\infty) = -\frac{\pi}{2}$, $\varphi(\infty) = \frac{\pi}{2}$, $\varphi'(-\infty) = \varphi'(\infty) = 0$. The magnetization state far from the domain wall is constant and in either the positive or negative y direction. Given these boundary conditions, the energy and the magnetization distribution can be determined with variational calculus by taking a functional derivative and finding dx.

Eq. 38 $$\frac{\delta\gamma_w}{\delta\varphi} = -2K_{u1}\sin\varphi\cos\varphi - 2A\varphi'' = 0$$

If Eq. 38 is multiplied by φ', it can be integrated with respect to x.

Eq. 39 $$\int [-2K_{u1}\sin\varphi\cos\varphi\,\varphi' - 2A\varphi'\varphi''] dx = 0$$

Eq. 40 $$K_{u1}\cos^2\varphi - A\varphi'^2 = C$$

Inputting the boundary conditions $\varphi(\infty) = \frac{\pi}{2}$ and $\varphi'(\infty) = 0$ gives C=0, and the result can be rewritten as

Eq. 41 $$K_{u1}\cos^2\varphi = A\varphi'^2$$

This can then be rearranged as follows to find dx:

Eq. 42 $$\varphi' = \frac{d\varphi}{dx} = \sqrt{\frac{K_{u1}}{A}}\cos\varphi$$

Eq. 43 $$dx = \sqrt{\frac{A}{K_{u1}}}\frac{1}{\cos\varphi}\, d\varphi$$

To find γ_w, combine Eq. 37, Eq. 41, and Eq. 43.

Eq. 44 $$\gamma_w = \int_{-\frac{\pi}{2}}^{\frac{\pi}{2}} [K_{u1}\cos^2\varphi + K_{u1}\cos^2\varphi]\sqrt{\frac{A}{K_{u1}}}\frac{1}{\cos\varphi}\, d\varphi$$

Eq. 45 $$\gamma_w = \int_{-\frac{\pi}{2}}^{\frac{\pi}{2}} [2\sqrt{AK_{u1}}\cos\varphi]\, d\varphi$$

Integrating Eq. 45 and solving gives an expression for the domain wall energy.

Eq. 46 $$\gamma_w = \left[2\sqrt{AK_{u1}}\sin\varphi\right]_{-\frac{\pi}{2}}^{\frac{\pi}{2}} = 4\sqrt{AK_1}$$

The magnetization distribution φ(x) can also be determined by integrating Eq. 43.

Eq. 47 $$x = \int \sqrt{\frac{A}{K_{u1}}}\frac{1}{\cos\varphi}\, d\varphi$$

Eq. 48 $$x = \sqrt{\frac{A}{K_{u1}}}\ln(\sec\varphi + \tan\varphi) + C$$

Applying an additional boundary condition, φ(0)=0, the integration constant, C, is found to be zero.

Eq. 49 $$x = \sqrt{\frac{A}{K_{u1}}}\ln(\sec\varphi + \tan\varphi)$$

Using the known identity that $\ln(\sec\theta+\tan\theta) = \tanh^{-1}(\sin\theta)$, Eq. 49 can be simplified and rearranged to solve for φ.

Eq. 50 $$x = \sqrt{\frac{A}{K_{u1}}}\tanh^{-1}(\sin\varphi)$$

Eq. 51 $$\varphi(x) = \sin^{-1}(\tanh(\frac{x}{\sqrt{A/K_{u1}}}))$$

The magnetization profile φ can be used to define the domain wall thickness. The wall thickness definition preferred here is the one proposed by Lilley [18]. Draw a line tangent to φ at x=0 and extend this tangent line to meet the boundaries at φ = π/2 and φ = -π/2. These intersections define the boundary of the domain wall. This is demonstrated visually in Figure 1.9. Taking the derivative of Eq. 51 at x = 0 gives a slope of $\frac{1}{\sqrt{A/K_{u1}}}$ for the tangent line. Finding the intersections of the tangent line gives a domain wall thickness, W, of $\pi\sqrt{A/K_{u1}}$. This definition can be applied similarly to domain walls with different magnetization profiles.

Describing 180° Bloch walls in a cubic material is somewhat more complicated. For a material with cubic anisotropy and <100> easy directions, the z-axis in Figure 1.8 is an easy axis in addition to the y-axis. This means that there is an orientation of minimum anisotropy energy in the center of the 180° wall. If only anisotropy and exchange energy are considered, the 180° wall can split into 90° walls separated by any distance without changing the total wall energy. Thus, the 180° Bloch wall appears to be unstable in cubic materials. This problem is solved by considering magnetoelastic effects. As was shown in Figure 1.6, a 90° wall orientated with the (100) plane has a large misfit strain and is elastically incompatible. However, 180° domain walls are always elastically compatible. It is for this reason that 180° walls exist in cubic materials.

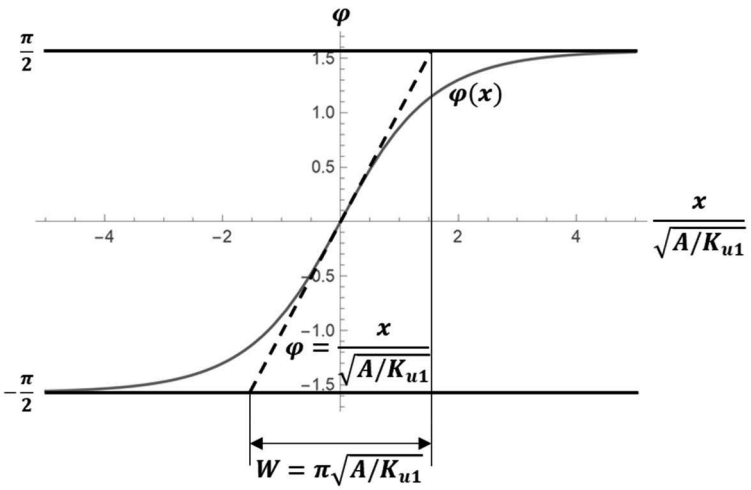

Figure 1.9: Plot of φ(x) vs. $\frac{x}{\sqrt{A/K_{u1}}}$ for a 180° Bloch wall in a uniaxial material. The tangent line at x=0 intersects with φ = π/2 and φ = -π/2 to define the wall thickness.

1.3.7 Zigzag Folding of 90° Domain Walls

Up to this point it has been assumed that all charge free 90° domain walls (those that satisfy Eq. 26) have equivalent wall energy unless elasticity is considered. However, when the wall energy is calculated this assumption is found to be incorrect. Utilizing the method laid out in section 1.3.6, the wall energy can be calculated for a 90° wall. The general method is the same. Define an integral for the wall energy, accounting for the exchange energy and the anisotropy energy, now using cubic anisotropy. The energy can be modified for walls of different angles, Ψ, but the path is defined such that the magnetization component perpendicular to the wall is always constant (an uncharged wall). Take a functional derivative to find an expression for dx (as in Eq. 43) and create an integral for the total wall energy (as in Eq. 45). For any arbitrary wall angle, Ψ, the integral must be solved numerically.

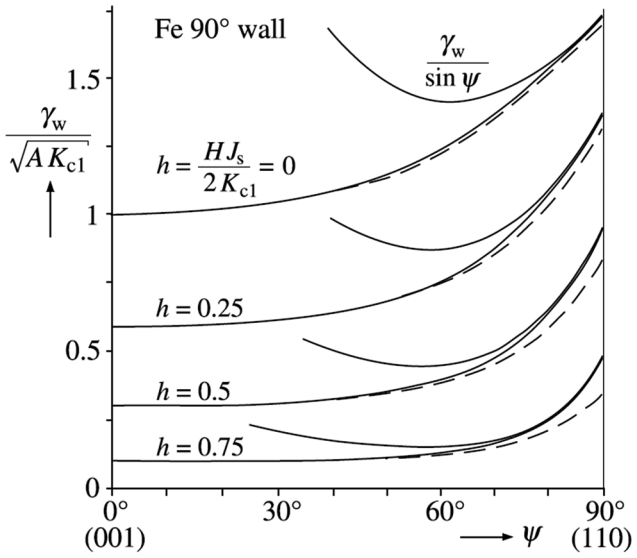

Figure 1.10: Plot of the normalized wall energy for 90° walls in iron with different orientations, Ψ. Different values of h represent applied fields in the [110] direction. The dashed lines represent deviations from stray field free paths. Zigzag folding causes an increase in wall area by 1/sinΨ. The curves of γ_w/sinΨ account for this area increase. From Hubert and Schafer with permission [17].

After performing this integration for multiple angles, the wall energy can be plotted as a function of Ψ. A plot of this type was given by Hubert and Schafer [17], presented here in Figure 1.10. The curves extending from the left axis to the right axis represent the normalized wall energy for different angles and different values of applied field, h, in the [110] direction. The wall energy is actually lowest for (001) oriented walls with Ψ = 0° and increases to a maximum at Ψ = 90°. This is because the magnetization path is longer for larger values of Ψ and comes closer to the [111] hard direction.

This sets up a competition between the anisotropy energy, which tends to prefer (001) walls, and the magnetoelastic energy, which tends to prefer (110) walls. The lowest energy state then is a wall with some intermediate orientation. Chikazumi and Suzuki [19] performed an analysis of domain walls of this type. They observed zigzag-shaped domain walls on the surface of Fe-Si single crystals in the vicinity of scratches and other surface defects. These zigzag lines were in fact not domain walls but V-lines, lines formed on the

surface by the meeting of two subsurface 90° domain walls (see Figure 1.11). This geometry is necessary to ensure that surface domains are parallel to the surface and flux closure is accomplished.

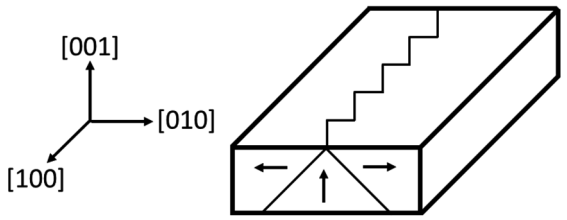

Figure 1.11: Subsurface structure of zigzag V-lines. The zigzag is formed by two 90° walls meeting at the surface.

The zigzag shape is a result of 90° domain walls deviating from the (110)-type planes, the (011) and $(0\bar{1}1)$ plane in the case of Figure 1.11. Figure 1.12 shows why this is the case. When the wall angle, Ψ, differs from 90°, the wall tips up towards the surface or down away from it, changing the angle of intersection. Chikazumi and Suzuki [19] define the angle between zigzag teeth as ω, so the angle shown is ω/2.

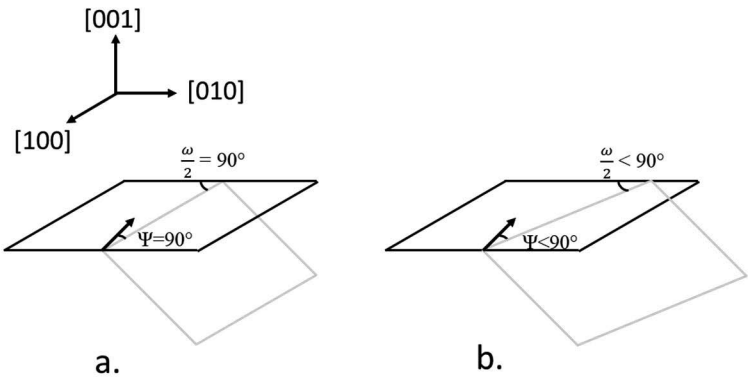

Figure 1.12: Relationship between the angles Ψ and ω for a 90° domain wall. When Ψ=90° the wall is on (011) and the line on the surface is along [100], (a). When the angle is less than 90° (b), the domain wall tips up and the line on the surface tilts.

In the case of the V-lines forming flux closure at the surface, the 90° wall is fixed to a (110) orientation. To minimize energy, the wall folds into a zigzag shape, allowing it to maintain the same average angle while also reducing the anisotropy and exchange energy. The folding introduces an extra energy cost because of the increase of wall energy caused be the increase in total surface area. The assumption made by Chikazumi and Suzuki [19] is that this increase in surface area by a factor of $1/\sin\Psi$ is the dominant energy controlling the angle of the domain wall. When this extra energy term is added to the wall energy the shape of the γ_w vs. Ψ plot changes, as seen on the right side of Figure 1.10. The result is a clear energy minimum. Once the angle Ψ is determined, it can be converted to ω by Eq. 52.

Eq. 52
$$\tan\left(\frac{\omega}{2}\right) = \frac{\tan\Psi}{\sqrt{2}}$$

The authors calculated an angle of ω=106° and measured angles from 103° to 109°, in good agreement with their predictions. Different values of K_1 and K_2 change the energy landscape which defines the optimal magnetization path, while the exchange constant, A, controls the wall thickness.

1.3.8 Effects of Elasticity on Zigzag Domain Structures

Classical models of the zigzag folded 90° domain walls consider the role of the magnetoelastic energy in the formation of these walls, but stop short of considering how elasticity influences the structure of these walls. Qualitatively, the effect of elasticity on the angle ω is apparent. In the presence of large stresses of magnetostrictive origin, larger angles will be preferred because stresses on the domain wall are reduced at higher values of ω, and by association Ψ, reduce elastic mismatch. This effect will not be discussed at length. In this section, a new model will be presented for the effect of the magnetoelastic energy on the thickness of the zigzag wall. In this case thickness refers not to the domain wall classical thickness but to the amplitude of the zigzag wave.

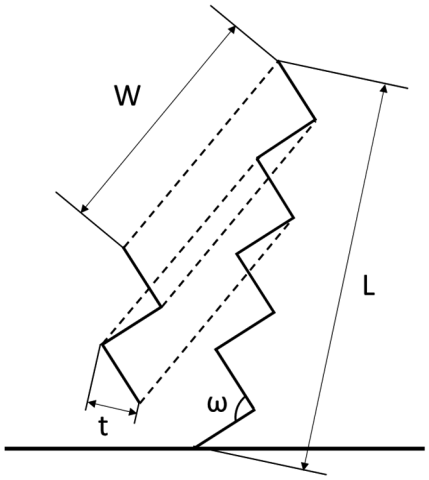

Figure 1.13: Definitions of zigzag wall dimensions. L is the length of the zigzag line on the surface. W is the wall width and represents how deep into the bulk the domain wall extends, measured along the relevant <110> direction. The thickness of the wall is given by t, equivalent to twice the amplitude of the zigzag wave.

This derivation treats the energy terms in a qualitative sense in order to determine a functional form of the influence of magnetostriction of the wall thickness. Figure 1.13 gives definitions for the domain wall length, width, and thickness. The elastic energy will be defined by Eq. 53, where μ is an elastic modulus, and λ is some magnetostriction constant.

Eq. 53 $$E_{elastic} = \mu\lambda^2 LWt$$

The elastically strained region is contained within the domain wall thickness, t. The surface energy is a function of the surface area, and is represented by Eq. 54.

Eq. 54 $$E_{surface} = \gamma_w \frac{LW}{\sin(\omega/2)}$$

The third energy term is the gradient energy, associated with the sharp kinks in the domain wall. It is represented by Eq. 55, where β is the gradient energy per unit length of the kink line and N is the number of kinks in the wall.

Eq. 55 $$E_{gradient} = \beta NW$$

The number of kinks is given by Eq. 56.

Eq. 56 $$N = \frac{L}{t\tan(\omega/2)}$$

Adding together all energy terms gives Eq. 57.

Eq. 57 $$E_{total} = E_{elastic} + E_{surface} + E_{gradient}$$
$$= \mu\lambda^2 LWt + \gamma_w \frac{LW}{\sin(\omega/2)} + \frac{\beta WL}{t\tan(\omega/2)}$$

This expression is then differentiated with respect to t.

Eq. 58 $$\frac{dE_{total}}{dt} = \mu\lambda^2 LW - \frac{\beta WL}{t^2\tan\left(\frac{\omega}{2}\right)} = 0$$

This is then solved for t.

Eq. 59 $$\mu\lambda^2 = \frac{\beta}{t^2\tan\left(\frac{\omega}{2}\right)}$$

Eq. 60 $$t^2 = \frac{\beta}{\mu\lambda^2\tan\left(\frac{\omega}{2}\right)}$$

Eq. 61 $$t = \frac{1}{\lambda}\sqrt{\frac{\beta}{\mu\tan\left(\frac{\omega}{2}\right)}}$$

The final result gives $t \propto 1/\lambda$, which is to say that materials with stronger magnetostriction will have thinner zigzag lines. This interpretation makes sense physically. When the 90° wall folds in alternating directions, the strain mismatch also alternates. At long distances from the wall there is an averaging effect and the magnetoelastic energy tends to zero. Only at small distances near the wall are the magnetoelastic effects felt

strongly. This averaging effect is more effective as the wavelength (and by association the thickness) of the zigzag becomes smaller. The shape of the zigzag line is then essentially a competition between elastic energy, which tends to prefer a thin, finely toothed line, and the gradient energy, which prefers to minimize the number of sharp corners. For strongly magnetostrictive materials the elastic energy has a stronger influence.

Note that this model is not at all effective at quantifying the energy state of the domain walls. Its value comes only in predicting the dependence of the geometry of the zigzag line of the magnetostrictive constants.

1.4 Structure and Properties of Galfenol

The remainder of this chapter will be dedicated to issues specifically relating to galfenol. Topics discussed will include the phase structure of Fe-Ga alloys, the origin of large magnetostriction, and a review of the known magnetic domain structures in this material.

1.4.1 Influence of Ga Concentration on Magnetostriction

Sufficient additions of Ga can increase the magnetostriction in Fe by a factor of ten, from 40 ppm for pure Fe to 400 ppm for annealed and quenched $Fe_{80.9}Ga_{19.1}$ [1]. The reason for this large increase is not understood, but a few hypotheses have been proposed. The influence of Ga concentration on magnetostriction must first be considered. Galfenol displays an intriguing composition dependence of the magnetostriction constants. Clark et al. measured the magnetostriction at a range of Ga concentrations from 0 to 35 at% Ga. Their results are summarized in Figure 1.14, which shows the tetragonal magnetostrictive constant, $(3/2)\lambda_{100}$, as a function of Ga concentration [1].

A few key observations were made from this data. There are two peaks in magnetostriction at about 17 and 27 at% Ga with a drop in magnetostriction in between. Also of interest, the magnetostriction is significantly enhanced by annealing and quenching, as compared so slow cooling. This shifts the first peak from 17 at% Ga to about

19 at% Ga. At 400 ppm, this is the highest magnetostrictive strain observed for these alloys. The first peak coincides with the peak in magnetoelastic coupling constant $b_1=-(3/2)\lambda_{100}(c_{11}-c_{12})$. The authors attribute the second peak to the softening of the elastic constant $c_{11}-c_{12}$, which decreases over the entire composition range [1].

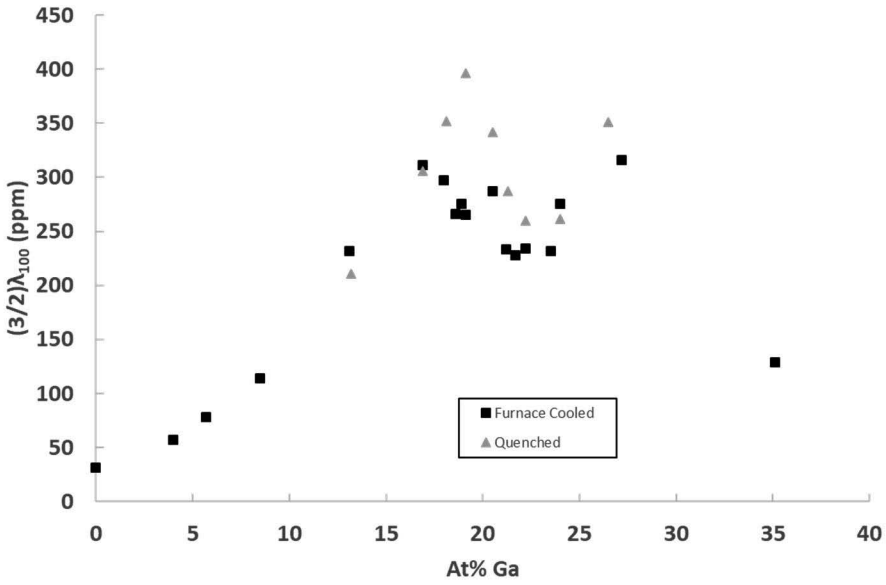

Figure 1.14: $(3/2)\lambda_{100}$ as a function of Ga concentration for $Fe_{100-x}Ga_x$. Data from Clark et al. [1].

It is helpful to consider the phase distribution in galfenol. The Fe-Ga equilibrium phase diagram by Ikeda et al. is shown in Figure 1.15 [20]. The iron BCC phase, A2, exists at low Ga concentrations. At higher concentrations a eutectoid equilibrium is formed between A2 and $L1_2$, an ordered FCC phase. However, $D0_3$, an ordered BCC phase, has significant metastability and will precipitate prior to $L1_2$ [20]. For this reason, it is more useful to consider the metastable phase $D0_3$. Figure 1.16 gives the metastable phase Fe-Ga phase diagram by Ikeda et al. [20]. Lograsso and Summers used X-ray diffraction to measure the phase fractions of A2 and $D0_3$ phases in quenched and slow cooled alloys with 19.5 and 22 at% Ga. They found that at 19.5 at% Ga resulted in single phase A2 when quenched, but formed 33% $D0_3$ when slow cooled. The 22 at% Ga alloy formed 60% $D0_3$ when quenched and single phase $D0_3$ when slow cooled [21]. This suggests that the drop in magnetostriction after 19 at% Ga is associated with the formation of the ordered $D0_3$

phase. Between 24 and 29 at% Ga the magnetostriction increases again, which corresponds to single phase $D0_3$ in the metastable phase diagram.

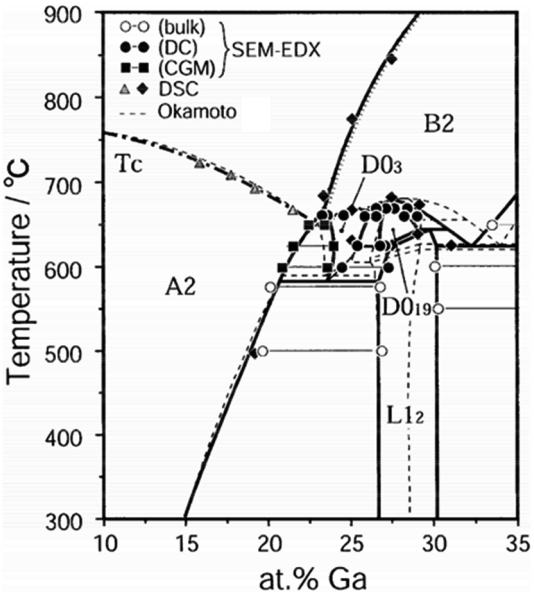

Figure 1.15: Equilibrium Fe-Ga phase diagram. From Ikeda et al. with permission [20], with data from Okamoto [22].

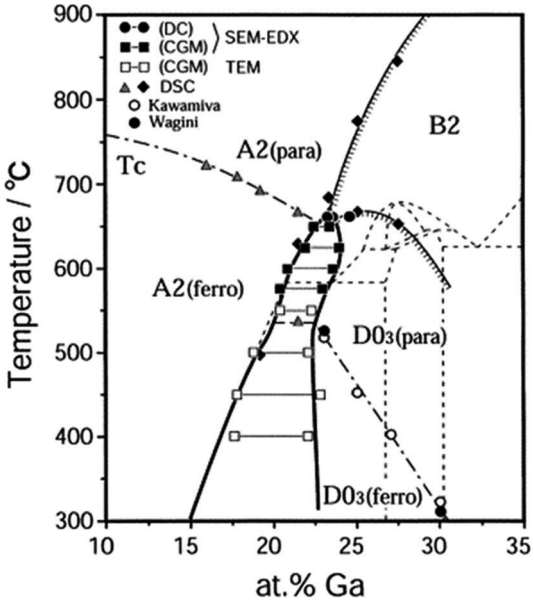

Figure 1.16: Metastable Fe-Ga phase diagram. From Ikeda et al. with permission [20], with data from Kawamiya et al. [23] and Wagini [24].

Xing et al. performed TEM studies of quenched and slow cooled alloys at a range of Ga concentrations [25]. For slow cooled alloys, single phase A2 existed up to the first peak. Formation of $D0_3$ was associated with a drop in magnetostriction. Single phase $D0_3$ increased in magnetostriction with increasing Ga content until the second peak. At compositions above the second peak, precipitates of another phase begin to form, associated with a drop in magnetostriction. The behavior was similar for the quenched alloys, except that samples with 25 and 29.9 at% Ga had a mixture of A2, B2, and $D0_3$. In general, it appears that the drop in magnetostriction after each peak is associated with the formation of a second phase, while magnetostriction increases with Ga content in single phase regions.

1.4.2 Mechanisms for Large Magnetostriction in Galfenol

The mechanism behind the exceptional magnetostriction in galfenol has not been confirmed, but there are two competing hypotheses. One possible explanation is short range ordering of Ga in the form of Ga-Ga atom pairs in the <100> directions. Cullen et al. suggest that the increase in magnetostriction is caused by short range ordering resulting in elastic softening [26]. Several authors have explored this idea in detail. First principles simulations by Wu et al. found that when some Ga atoms were removed from ordered regions, producing nonuniform distribution of Ga atoms, the magnetostriction increased [27]. Paduani and Bormio-Nunez used first principles calculations with density functional theory to show that the presence of <100> aligned Ga-Ga pairs produced an increase in magnetostriction [28]. Pascarelli et al. performed X-ray studies on galfenol to analyze short range ordering and found some evidence of Ga-Ga pairing in the structure but no evidence of clustering [29]. First principles calculations by Wang et al. were able to reproduce the elastic softening observed by Clark et al. and attributes it to weakening of Fe-Fe bonds in <100> due to separation by an Fe-Ga mixed layer [30]. In general, good experimental data is difficult to produce. Even with the x-ray techniques it is difficult to measure the effects of short-range ordering. Only a few techniques are capable of directly measuring the atomic

positions. Atom probe tomography and high resolution transmission electron microscopy are some of the few techniques capable of taking measurements on the appropriate scale.

Khatchaturyan and Viehland proposed an alternative mechanism for increase magnetostriction in galfenol [31]. They suggest that $D0_3$ formation is stabilized in part of the single phase A2 region by absorption of quenched-in vacancies, forming a dispersion of nanoprecipitates. The $D0_3$ precipitates distort to form a face centered tetragonal (FCT) phase. In this case the large magnetostriction is a result of magnetically induced reorientation of twin variants in the FCT precipitates [32]. The drop in magnetostriction with $D0_3$ formation is explained by the rapid growth of $D0_3$ allowed in the stable region. The growth of large particles of $D0_3$ prevents the formation of FCT nanoprecipitates.

1.4.3 Domain Structures in Galfenol

Regarding magnetic domains in galfenol, little work has been done to investigate the full range of domain structures. Existing studies usually examine domains for one composition, and on one crystallographic plane. Bai et al. demonstrated a series of stripe or maze domain structures in galfenol alloys with a size of a few microns [33, 34]. Many other authors [35-44] have reported similar structures. These observations account for the bulk of the literature on magnetic domains in galfenol. More detailed analysis by Mudivarthi et al. [45] showed that these maze domains were not the true domain structure. They were caused by surface stresses induced by mechanical damage from surface polishing. After adding an additional polishing step with colloidal silica or etching with 10% Nital, the domains changed to a stair step structure with regular 90° and 180° domain walls and a domain size of tens of microns. These were traditional flux closure domain structures. This effect was observed for single crystals of $Fe_{82.5}Ga_{17.5}$ under slow cooled and quenched conditions and $Fe_{81}Ga_{19}$ under a quenched condition.

In actuality, the maze domain structures seen by many authors were not dissimilar to the zigzag structures seen in Fe-Si alloys by Chikazumi and Suzuki [19]. They observed maze-like structures on surfaces with induced surface stresses from polishing. They

showed that electropolishing could remove the surface layer and reveal flux closure domain structures with 90° and 180° domain walls. It was also observed that the concentration of the ferrofluid was critical in observing the zigzag shape of the domain walls. If the ferrofluid was not diluted sufficiently, excessive buildup of particles would smooth out the features of the domain wall, giving maze-like structures with apparently smooth walls.

In general, zigzag lines are the result of some sort of stress. Chikazumi and Suzuki [19, 46], as well as Bates and Carey [47] observed a maze of zigzag lines on surfaces with polishing induced stresses. Hubert and Schafer [17] reported on zigzag lines on a crystal of Fe-Si under the influence of a compressive planar stress. This structure is preferred by compressive stresses as a result of magnetostriction. Domains magnetized along the axis of the compressive stress are not favored because they tend to expand along that direction. Alternatively, the magnetoelastic energy can be reduced by magnetizing perpendicular to the surface, since this results in contraction along the compressive stress direction. The stress effectively induces a uniaxial anisotropy. However, the surface cannot tolerate this perpendicular magnetization due to production of stray fields. Zigzag V-lines are necessary to complete flux closure of the perpendicularly magnetized domains below.

Mudivarthi et al. were not the only ones to observe charge-free 90° and 180° domain walls in galfenol. Asano et al. observed similar domains on a (001) plane of single crystal $Fe_{83.9}Ga_{16.1}$ and documented their motion under applied fields [48]. The 180° domain walls were observed to move first, and the 90° domain walls, associated with magnetostriction, moved second. Stair step domains were also observed by He et al. [49]. Raghunath and Flatau overserved domains on the (001) plane of single crystal $Fe_{84.2}Ga_{15.8}$ and saw parallel bar domains with 180° domain walls [50]. Near the sample edge, closure domains with 90° and 180° domain walls were observed.

Some work has been done on domain structures under applied stress. Song et al. observed domains in polycrystals of $Fe_{81}Ga_{19}$ and found that the domains aligned perpendicular to an applied uniaxial compressive stress [38]. Raghunath et al. observed parallel bar domains with 180° domain walls in galfenol whiskers. The domains rotated

under applied bending stresses, specifically in areas that were under compression [51]. Parkes et al. were able to cause a 90° rotation in the magnetization of a galfenol thin film through the application of tensile stresses [52].

Of particular interest are the fascinating domain structures observed by Chopra and Wuttig in the (001) plane of annealed and quenched $Fe_{73.9}Ga_{26.1}$ [11]. It contained what they referred to as a cellular structure, bands of rectangular "cells" with highly regular dimensions and long-range periodicity. Each cell was surrounded by zigzag lines and was divided into four sections. The authors interpreted each cell as containing a closure loop. Their interpretation is recreated in Figure 1.17. They appeared similar to typical closure domains with 90° and 180° domain walls forming a closed loop, but such a structure with zigzag walls is unusual. This choice of interpretation is interesting given that the classical model of Chikazumi and Suzuki [19], and its reproduction by Hubert and Schafer [17], neatly describe these types of structures as V-lines. The bands of cells reorient by 90° when a field is applied parallel to the band such that these bands are always perpendicular to the applied field.

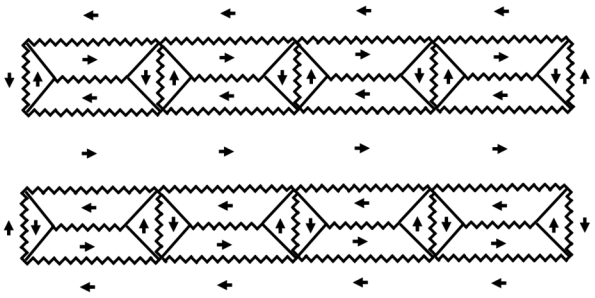

Figure 1.17: "Cellular" magnetic domains as interpreted by Chopra and Wuttig [11]. Each "cell" was interpreted as a closure loop with the magnetization always parallel to the zigzag lines.

The authors suggest that the magnetization is not uniform within the cells and that the periodicity results from strain modulation originating from charge density waves. In this interpretation the magnetization varies so that, locally, it is somewhat parallel to the edges of the zigzag teeth. They claim that magnetostriction in certain galfenol alloys is not

volume conserving and that the modulated strain state is the cause. This non volume conserving property contradicts the classical observation by Joule [53] that volume is constant with magnetostriction, leading to the term "non-Joulian magnetostriction."

Chopra also demonstrated in a slow cooled sample of $Fe_{73.9}Ga_{26.1}$ that the domain structure formed a perfect mirror image across the whole sample with a bisector moving down the centerline [54]. This sample demonstrated volume conserving magnetostriction. The authors believe the non-volume conserving property depends on long range periodicity which they only observed in quenched samples. The same non-volume conserving behavior was observed in Fe-Ge and Fe-Al alloys [55].

Dabade et al. [56] were able to create a complex micromagnetic model of the periodic magnetic and elastic state proposed by Chopra. He et al. [49, 57] attempted to confirm Chopra's claims of non-Joulian magnetostriction. They measured magnetostriction in quenched and slow cooled $Fe_{83}Ga_{17}$ and could not reproduce the non-volume conserving magnetostriction. In reference [57] the volume was measured directly by placing the galfenol crystal in a flask of alcohol connected to a capillary tube and measuring the level of the liquid while applying magnetic fields.

While the promising work of Chopra shows that there are rich magnetic domain structures to be explored in galfenol, few authors have explored anything but simple, stress-induced maze domains. The goal of the experiments presented in this work will be to more fully explore the available domain structure in these alloys, and also to better explain the complex and poorly understood cellular structure. As a note, for the rest of this work the so-called cellular domain structure will be referred to as chain domains. As will be discussed more fully in Chapter 5, this name is preferred because it was used in older works to describe similar structures in Fe-Si alloys.

2 Experimental Methods and Instrumentation

2.1 Introduction

This chapter will briefly discuss the surface preparation methods employed, the relevant domain observation techniques, and the development of electromagnet coils for the application of in situ magnetic fields.

2.2 Surface Preparation

Care must be taken during polishing to ensure that the surface is stress free and has minimal scratching. There are many surface preparation routes which could be taken. Mudivarthi et al. [45] and Chopra and Wuttig [11] had effective methods for preparing galfenol single crystals for domain observation. The methods used here will differ from those used by other authors, but they were found to produce a surface of exceptional quality when applied with patience. The approach will be described briefly, but the interested reader can find a more detailed standard operating procedure in Appendix A.

Polishing was performed with an Allied High Tech LaboPol-1 autopolisher. Samples were mounted in Allied High Tech EpoxySet epoxy (but another slow setting, high hardness epoxy will suffice). The following materials were used:

- PSA backed SiC paper discs, 600 and 800 grit (8 inch)
- Allied High Tech White Label Flexible Back Magnetic 8 inch disc
- Allied High Tech Imperial Flexible Back Magnetic 8 inch disc
- Buehler Microclotch Magnetic 8 inch disc
- Allied High Tech 1 μm Monocrystalline Diamond Compound
- Allied High Tech 0.04 μm Colloidal Silica Suspension
- Allied High Tech RedLube

Galfenol single crystals were first mounted in epoxy. A neodymium disc magnet was placed below the mount cup to hold the sample flat. The top surface of the mount cup base

was flattened on a grinding wheel to produce sample mounts with a flat surface. These steps were taken to minimize the epoxy that needed to be removed before reaching the sample surface. Without these steps, longer polishing times will be required on the first polishing step and the surface may be polished at a slight angle.

The sample was then polished using the following steps with a pressure of 15 N:

1. 600 grit SiC with continuous water lubrication
2. 800 grit SiC with continuous water lubrication
3. 1 μm monocrystalline diamond on Buehler Microcloth with RedLube
4. 0.04 μm colloidal silica on Allied High Tech White Label pad
5. 0.04 μm colloidal silica on Allied High Tech Imperial pad

The pads and polishing compound used here were found to be effective, but substitutions can be made for equivalent abrasives and pads with similar textures.

It is worth noting that electropolishing could be a better method of surface preparation. Electropolishing was not attempted in this work for fear of excessive material removal on precious single crystals. However, with proper expertise and the appropriate methods, electropolishing could produce a stress-free surface of the highest quality.

2.3 Instrumentation

The experiments in this work necessitated the development of electromagnet coils for application of in-situ magnetic fields under an optical microscope. This section will discuss some of the important considerations to be taken when designing electromagnets and which designs were selected for this work.

An electromagnet is a combination of a conductor (usually copper wire) wrapped around a ferromagnetic core (usually iron). The magnetic field, H, generated by a solenoid coil (with no core) is given by Eq. 62 [58].

Eq. 62 $$H = \frac{ni}{L}\left[\frac{L+2x}{2\sqrt{D^2+(L+2x)^2}} + \frac{L-2x}{2\sqrt{D^2+(L-2x)^2}}\right]$$

The current is given by i. The number of wire turns is n. The length and average diameter of the coil are L and D respectively. The field is given at a distance x from the center of the coil, measured along its centerline. This equation presents many of the variables to be considered in electromagnet design. Increasing the current or the number of turns will increase the field. Increasing the length or diameter decreases the field if the current and turns are held constant. However, the number of turns is not independent of the coil dimensions. They are linked through another important variable: the wire diameter. For a given wire diameter, the length or diameter increase with the number of turns.

Another factor to consider is the resistance of the coil. The coil resistance will affect the voltage required to produce a given current. It also influences the heat generated by the coil. Coils with more resistance produce less current for a given voltage and heat up more quickly. Coils with more turns (more total wire length) and with smaller wire diameters will have more resistance.

One more factor to consider, possibly the most important, is the iron core. The core is magnetized by the field from the coil, multiplying the magnetic field. The effectiveness of the core is very sensitive to geometry as a result of the demagnetizing field (stray field). Cylinders with large faces are difficult to magnetize because they produce large magnetic poles, and thus large demagnetizing fields. Longer cylinders are easier to magnetize because of volume effects. The demagnetizing field, H_d, can be determined by simplifying these effects into a demagnetizing factor, N_d, as shown in Eq. 63, where M is the magnetization.

Eq. 63 $$H_d = -N_d M$$

Demagnetizing factors for cylinders with different aspect ratios were compiled by Chen et al. [59], but in general, longer and thinner cores are more easily magnetized and produce larger magnetic fields. Thinner core material is always preferred as long as a uniform field can be maintained.

The design of electromagnets is then a complex process of maximizing magnetic field while optimizing a series of geometrically interrelated variables: coil length, coil diameter, core length, core diameter, wire diameter, number of turns, current, and resistance. This problem is simplified by applying a series of constraints. There were two major constraints for this application. The first was geometric. The coil and a galfenol single crystal sample had to fit in the working space beneath the microscope. This limited the coil length to about 7 cm. The second constraint came from the power supply, which could only supply 10 V.

These constraints helped limit the design space. An iron rod with a diameter of 10 mm was used as the core, just over twice the size of the 4 mm long samples. A spool was 3D-printed from PLA to wrap the coil around. It was 7 cm long with a 1 cm hole through the center to accommodate the core. After some initial screening tests, three coils were made using wire thicknesses of 18 AWG, 20 AWG, and 22 AWG. The 18 AWG wire was the thickest and produced a large coil for a small number of turns. This coil, 70 mm in diameter with 786 turns, produced a 2300 G field but was too bulky to be practical. The 20 AWG coil produced a similar field, 2200 G, using less material. It was 40 mm in diameter with 1210 turns. The 22 AWG coil was 40mm in diameter with 1782 turns. It produced the strongest field of all of the coils, but it became so hot that there was risk of melting the PLA with extended use. The coil made with 20 AWG wire was selected for use. Figure 2.1 shows an image of this coil before insulation was added.

Figure 2.1: Electromagnet coil made with 20 AWG copper wire.

2.4 Imaging Methods

Imaging was performed using the classic Bitter technique, developed by Francis Bitter [60] for the first observation of magnetic domains. A ferrofluid, a suspension of magnetite nanoparticles, was placed on the sample surface and then covered with a thin glass coverslip. The particles are drawn to the domain walls by stray fields produced at the intersection of domain walls with the surface. To enhance the visibility of the domain walls, interference contrast (IC) microscopy was used. A Nomarski prism enhances any height contrast from surface features on the sample. This makes domain walls more clearly visible by improving the visibility of magnetite particles built up at the wall. For this work, Ferrotec EMG707 water-based ferrofluid with a particle size of 10 nm was used. A 30:1 dilution with distilled water was found to produce good contrast in most cases.

When out-of-plane magnetic fields were required, the sample, mounted in epoxy, was placed on top of the electromagnet coil. The DC power supply was automated to ramp up the current linearly. To measure the field, three calibration curves were first collected. A gaussmeter probe was placed on top of the sample and the field was ramped up to maximum while a data acquisition system simultaneously measured the current and the magnetic field. The data was used to generate curves of magnetic field vs. current.

To observe domain evolution under applied fields, the gaussmeter was removed and videos were recorded while the field was automatically ramped up and down and the current was simultaneously measured. The calibration curves were used to convert the measured current into a magnetic field. The LAS-EZ software used for imaging was limited to collecting 30 seconds of video at a time. When slower ramp times were required, the field was ramped up in multiple steps. It would be increased for 30 seconds while collecting video and then held constant before being increased again for another video. This sometimes produced some discontinuities where two videos meet due to the relaxation time, but this did not affect the quality or value of the data in most cases.

Imaging was performed on the (100) plane of several single crystal samples including as-grown $Fe_{91}Ga_{8.5}$, as-grown and quenched $Fe_{85}Ga_{15}$, as-grown $Fe_{82.9}Ga_{17.1}$, and as-grown $Fe_{78.1}Ga_{21.9}$.

3 Closure Domains

3.1 Introduction

This chapter will explore structures of charge-free closure domains in galfenol single crystals.

3.2 Results and Discussion

The easiest domain structures to interpret were those seen on the (001) surface of as-grown crystals of $Fe_{85}Ga_{15}$. As shown in Figure 3.1, all of the domain walls have (100)- and (110)-type orientations, as would be expected with charge free 180° and 90° domain walls respectively. The relative domain orientations can be inferred from the wall orientations as illustrated. The charge free domain walls can combine in a variety of ways to form more complex structures, like the diamond-shaped structure seen in Figure 3.2. The relative domain orientations of these more complex structures can be analyzed in a similar fashion.

These domains are of the type reported by Mudivarthi et al. [45] (and other authors discussed earlier) after modifying polishing procedures to remove polishing induced surface stresses. While there is nothing remarkable about the interpretation of these domain structures, their presence is a good sign of proper surface preparation. Good surface quality can be achieved by silica polishing alone, without the need for an etchant. This is because the silica has a high pH, causing a chemical attack of the surface during polishing. This results in a mild chemical polishing effect in addition to mechanical polishing.

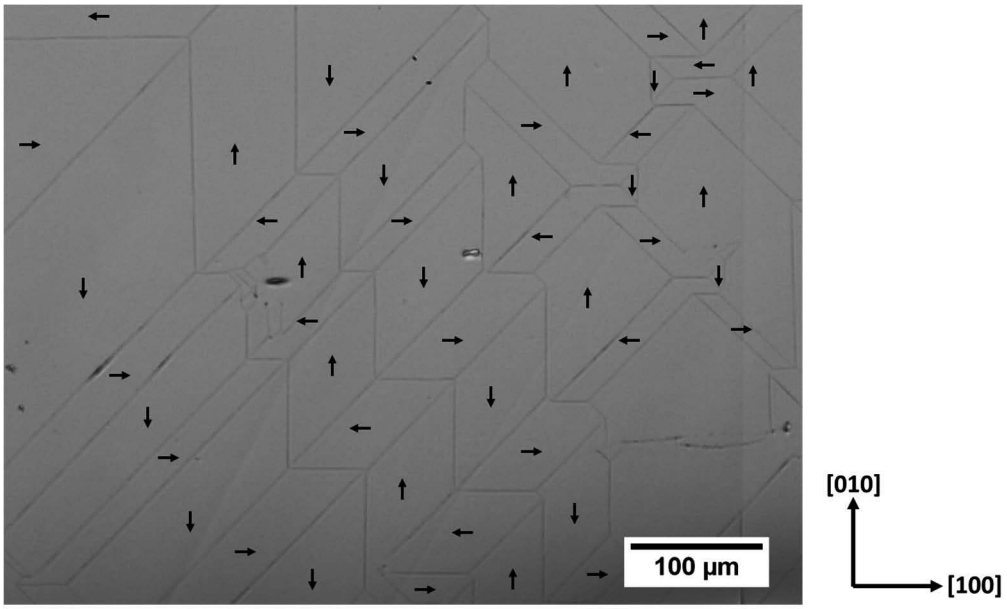

Figure 3.1: Head to tail flux closure domain structure with charge free 90° and 180° domain walls on a (001) surface of a single crystal of $Fe_{85}Ga_{15}$ in the as-grown state.

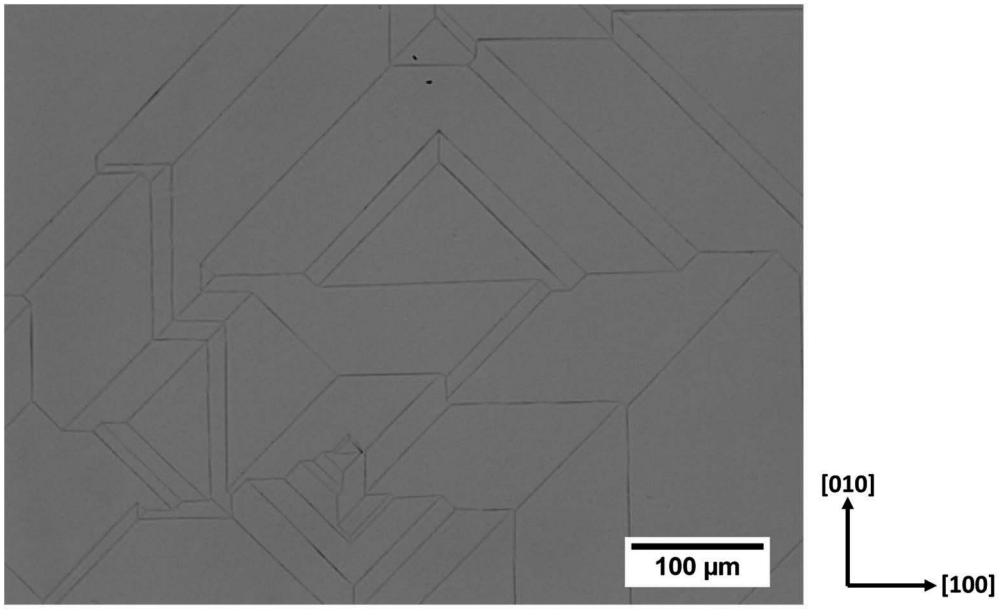

Figure 3.2: Complex structures of charge free 90° and 180° domain walls on a (001) surface of a single crystal of $Fe_{85}Ga_{15}$ in the as-grown state.

3.3 Conclusions

A series of polishing steps was selected for single crystals of galfenol. This method produced high quality surfaces for Bitter method imaging. The observation of simple stairstep-like closure domains made by Mudivarthi et al. [45] was repeated here, demonstrating that the a final polish with colloidal silica is sufficient to remove the stressed surface layer and prevent the formation of maze domains.

4 Charged Domain Walls

4.1 Introduction

In some cases, domain walls with a net magnetic charge are preferred by the material despite the increased magnetostatic energy. Several such structures occur in galfenol. Domain walls like this can form at the surface of the material as a result of surface effects. These include 90° and 180° domain walls with "head-to-head" and "tail-to-tail" orientations. This chapter will discuss the magnetization state of these domain patterns and the complex three-dimensional structures that they form.

4.2 Results and Discussion

4.2.1 Zigzag Domain Walls

One structure that occurs frequently in galfenol is the zigzag domain wall. Figure 4.1 shows a mixture of typical domain walls and zigzag domain walls. If the uncharged 90° and 180° domain walls are interpreted as usual, it can be shown that the zigzag walls at the top of the image are 180° walls with head-to-head and tail-to-tail orientations. This unusual orientation can be explained, as discussed in section 1.3.7, by interpreting the head-to-head and tail-to-tail domains as providing flux closure for subsurface domains with magnetizations perpendicular to the surface. This is illustrated schematically in Figure 4.2. The zigzag line is formed by the meeting of two subsurface 90° domain walls meeting at the surface to form a "V-line." This orientation prevents the formation or surface domains with magnetizations perpendicular to the surface. The zigzag V-lines are formed at the meeting of three domains and there is always an imbalance between magnetizations pointing toward the line and magnetizations pointing away from the line. This means that the lines at the surface always have a small net magnetic charge. However, the 90° domain walls that form the V-line are uncharged, with the charge being limited to a narrow region

at the surface. The energy associated with the charged line is insignificant compared to the energy savings afforded by the closure domains.

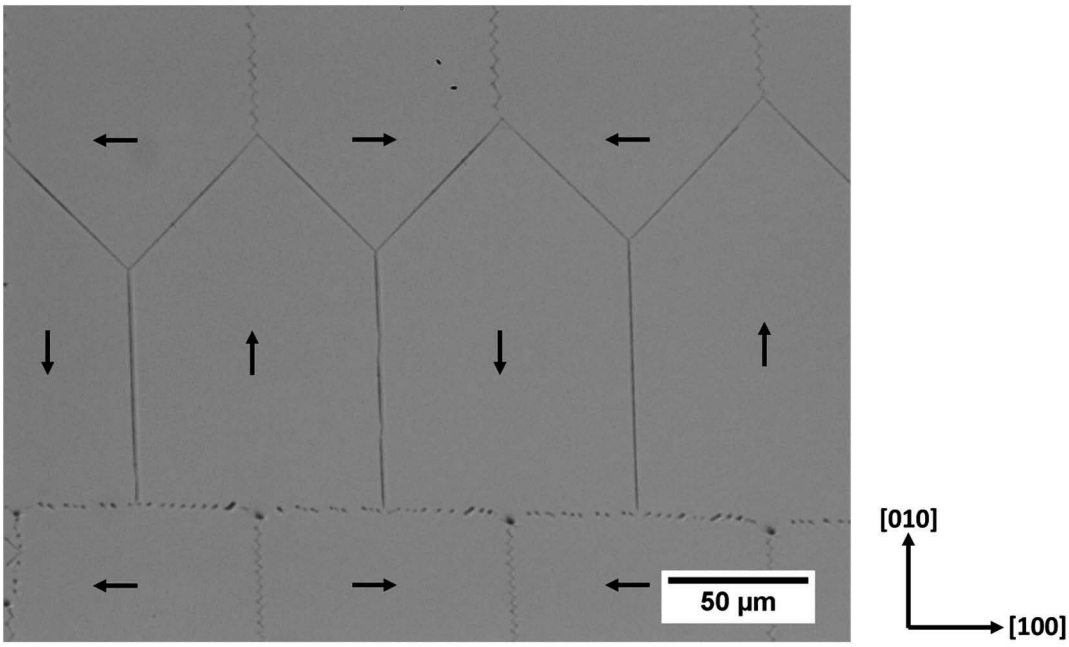

Figure 4.1: (001) surface of $Fe_{91.5}Ga_{8.5}$ with a mixture of charged zigzag domain walls and uncharged 90° and 180° domain walls.

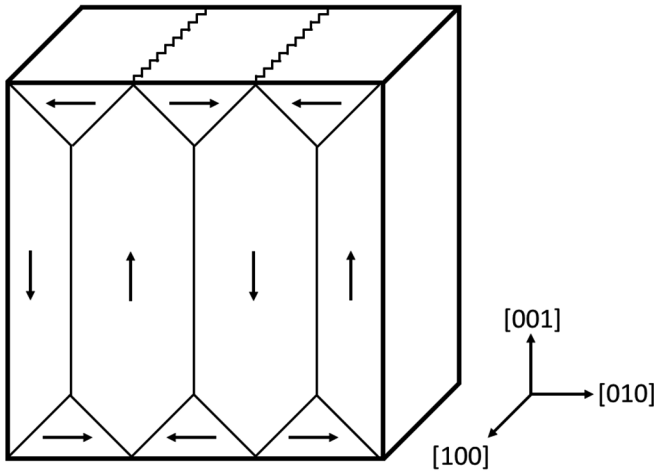

Figure 4.2: Diagram of a zigzag V-line. Zigzag lines are formed by the meeting of two subsurface 90° domain walls, producing a "V-line." The surface domains provide flux closure for subsurface domains magnetized perpendicular to the surface.

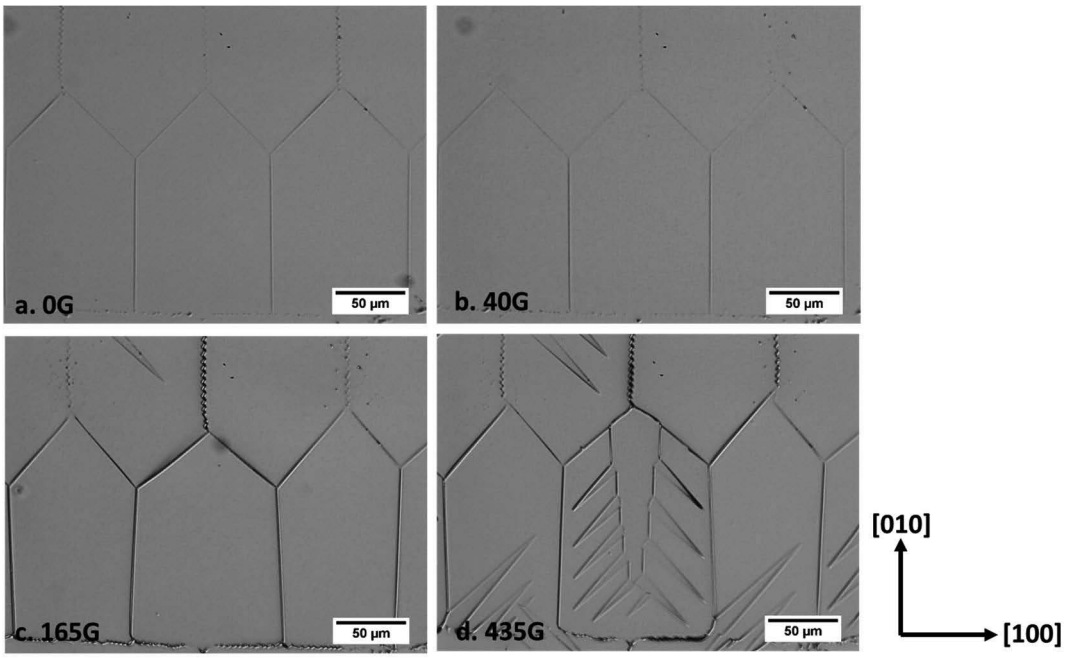

Figure 4.3: Response of zigzag V-lines to an out-of-plane magnetic field. At zero magnetic field (a) there are 3 zigzag lines visible. Applying a small field causes every other zigzag line to disappear. At higher fields (c) the invisible lines reappear and the remaining line gets darker. The lines which reappeared also become darker with increasing field (d).

Determining the orientations of the domains at the bottom of Figure 4.1 is made more complicated by the presence of an apparent 90° zigzag wall at the base of the pentagonal structure. More clarity can be provided by observing how this structure responds to magnetic fields applied out of plane. One clue can be found in the way these out-of-plane field affect zigzag V-lines, as seen in Figure 4.3. A small applied field causes every other zigzag line to disappear in an alternating pattern, while the remaining lines get darker. The invisible lines reappear at higher magnetic fields, and also get darker with increasing field. This behavior can be understood by examining the internal structure of the domain wall itself. Figure 4.4a and b show a cross section of two different V-lines at the surface. When an out-of-plane field is applied, domain walls with out-of-plane orientations become wider as the field applies an upward torque on the magnetic moments within the wall. Domain walls oriented into the plane have the opposite response and get narrower. This asymmetric response causes differences in the stray field distribution

around the zigzag lines, which also affects the response of the ferrofluid. When the applied field becomes large, regions of the narrowed wall begin to magnetize out of plane and the line gets wider again.

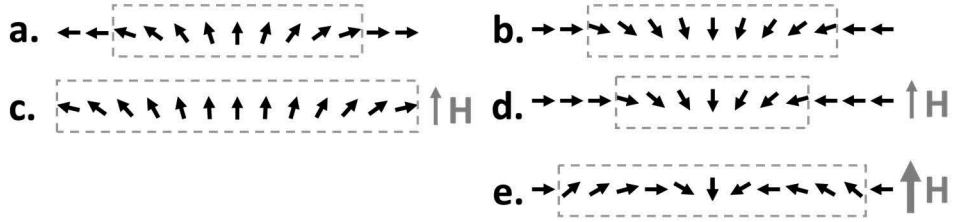

Figure 4.4: Response of V-lines to applied magnetic field. With no field applied, V-lines have structures like in (a) and (b). When a field is applied out of plane, domain walls with out-of-plane orientations become wider (c), but domain walls oriented into the plane become narrower (d). At high fields (e) the narrower wall becomes wide again as it begins to rotate out of plane.

When the direction of the field is reversed, the response of the zigzag lines is also reversed. The lines which previously remained visible disappear under a reversed field, and the lines which previously disappeared remain visible. This shows more clearly that orientation of the domain wall influences which lines disappear and which ones remain. This fact can be used to determine the orientations of the domains at the bottom of Figure 4.1. Figure 4.5 shows a lower magnification image of this structure with a small field applied out of plane. The zigzag V-lines above and below the pentagonal domains disappear in pairs, suggesting they have the same orientations. This supports the interpretation given in Figure 4.1 with the domains at the top and bottom of the image having the same orientations. The base of the pentagon structure is a zigzag 90° domain wall. This wall is unlike the 180° zigzag V-lines, despite its similar appearance. One unique feature of the 90° zigzag wall is that only one side of each zigzag tooth is clearly visible, while the other half is faint or invisible. This is a feature which will be elaborated upon in section 4.2.3.

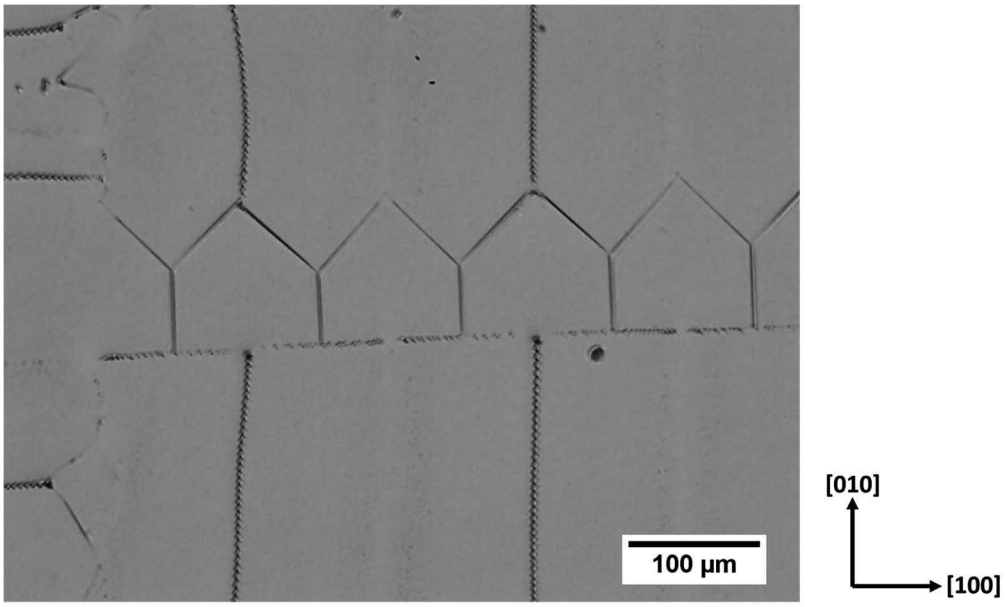

Figure 4.5: Low magnification view of pentagonal domain structures with an out-of-plane field of 140G. Zigzag lines above and below the pentagonal structures disappear as pairs.

A variation on the pentagonal domains can be seen in Figure 4.6. Instead of pentagons with 180° domain walls, simple triangle structures are formed. These structures are separated from each other so that the domains with horizontal [100] magnetizations are continuous from top to bottom. On the right side of the image a transitional structure can be seen. When the triangular domains come close enough to touch, a vertical 180° domain wall is formed, more like the pattern seen in Figure 4.1.

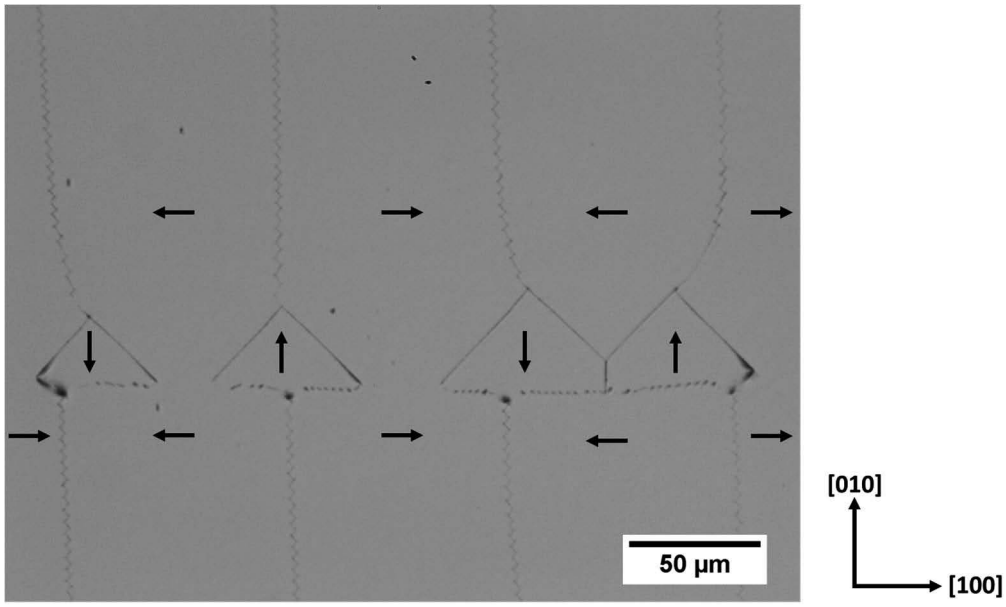

Figure 4.6: (001) surface of $Fe_{91.5}Ga_{8.5}$ with triangular domains. When the triangular domains grow close enough to touch, they can merge to form pentagons.

4.2.2 Domains formed under applied fields

When a magnetic field is applied perpendicular to the sample surface, spike and fir tree domains are formed. An analysis of these domain structures can help in determining useful information about the magnetization state of the basic domain structure. Figure 4.7 shows domains formed on the $Fe_{91.5}Ga_{8.5}$ with a magnetic field applied out of plane. These domains have a variety of structures with varying degrees of complexity. Figure 4.8 (a-d) shows a range of possible structures, from single spikes, to branched spikes, to fir tree domains with branches growing from a "trunk." The spikes form as a result of domains magnetized perpendicular to the surface, which nucleate as a result of the applied field. The spikes seen on the surface form flux closure, to ensure that the surface magnetization remains in plane. Figure 4.8e and f are interpretations of the subsurface structure shown in a and b, respectively, if they were cross sectioned through the dashed line. The domain walls of the spikes form angles that deviate slightly from the charge free (110) orientations, resulting in a surface charge. This charge is minimized by spreading out into a thin spike to approximate a 45° angle.

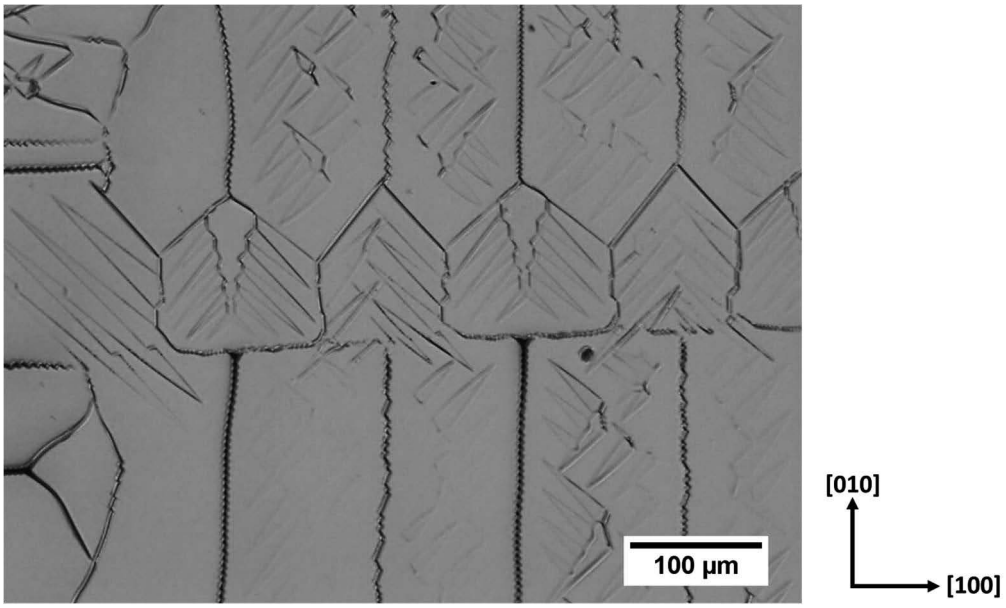

Figure 4.7: Spike and fir tree domains formed on a (001) surface of $Fe_{91.5}Ga_{8.5}$ with a 625G magnetic field applied perpendicular to the surface in the [001] direction

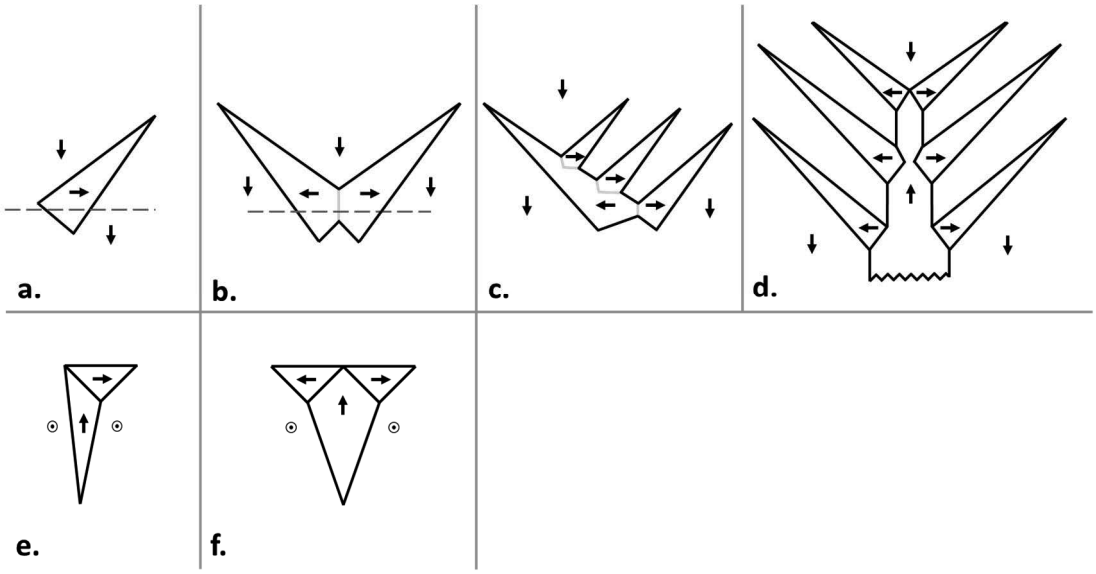

Figure 4.8: Domains formed under an out-of-plane field. The domains range in complexity from single spikes (a), to paired spikes (b), to branched spikes (c), and fir tree domains with a trunk and branches (d). The schematics in (e) and (f) show a cross section through the dashed line in (a) and (b) respectively.

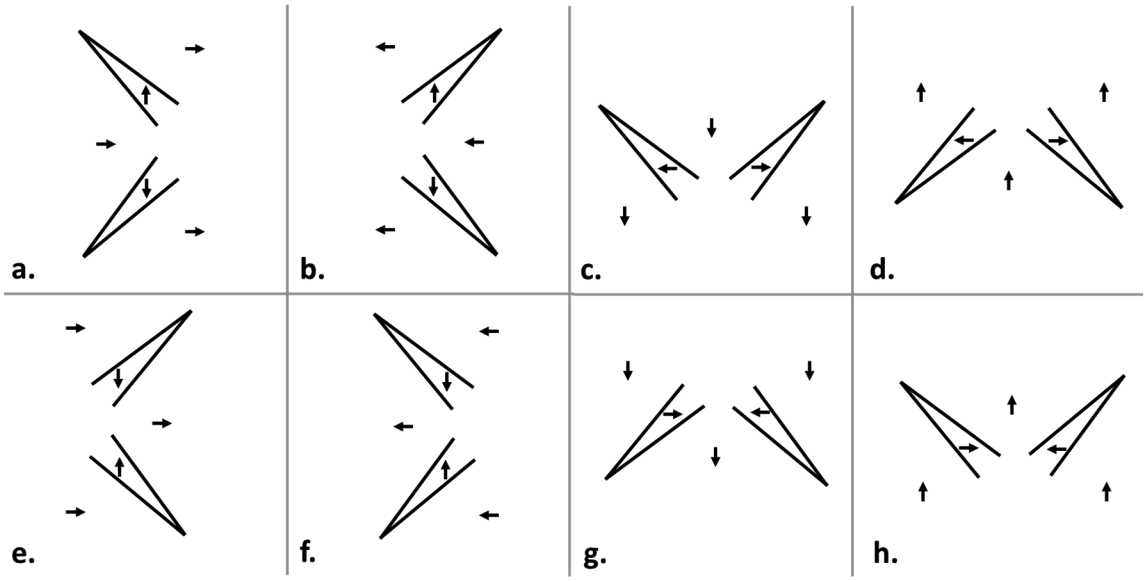

Figure 4.9: Possible orientations of spike domains. The possible orientations depend on the direction of the domain they grow from and the direction of the applied field. Structures (a-d) are favored when a field is applied out of plane and (e-h) are preferred when the field is applied into the plane.

Because the spikes form to accommodate domains with out-of-plane magnetizations, they occur at predictable angles. They always form in an orientation that will guide the flux out from the subsurface domain. The spikes can only point in two directions, and those directions are controlled by the magnetization of the domain that they grow from. Spike orientation is function only of the parent domain magnetization and the direction of the applied field. All of these possible orientations are shown in Figure 4.9. If the field is applied out of the plane in the [001] direction, the spike orientations in Figure 4.9a-d are favored. For a field applied into the plane in the $[00\bar{1}]$ direction, the orientations in Figure 4.9e-h are preferred.

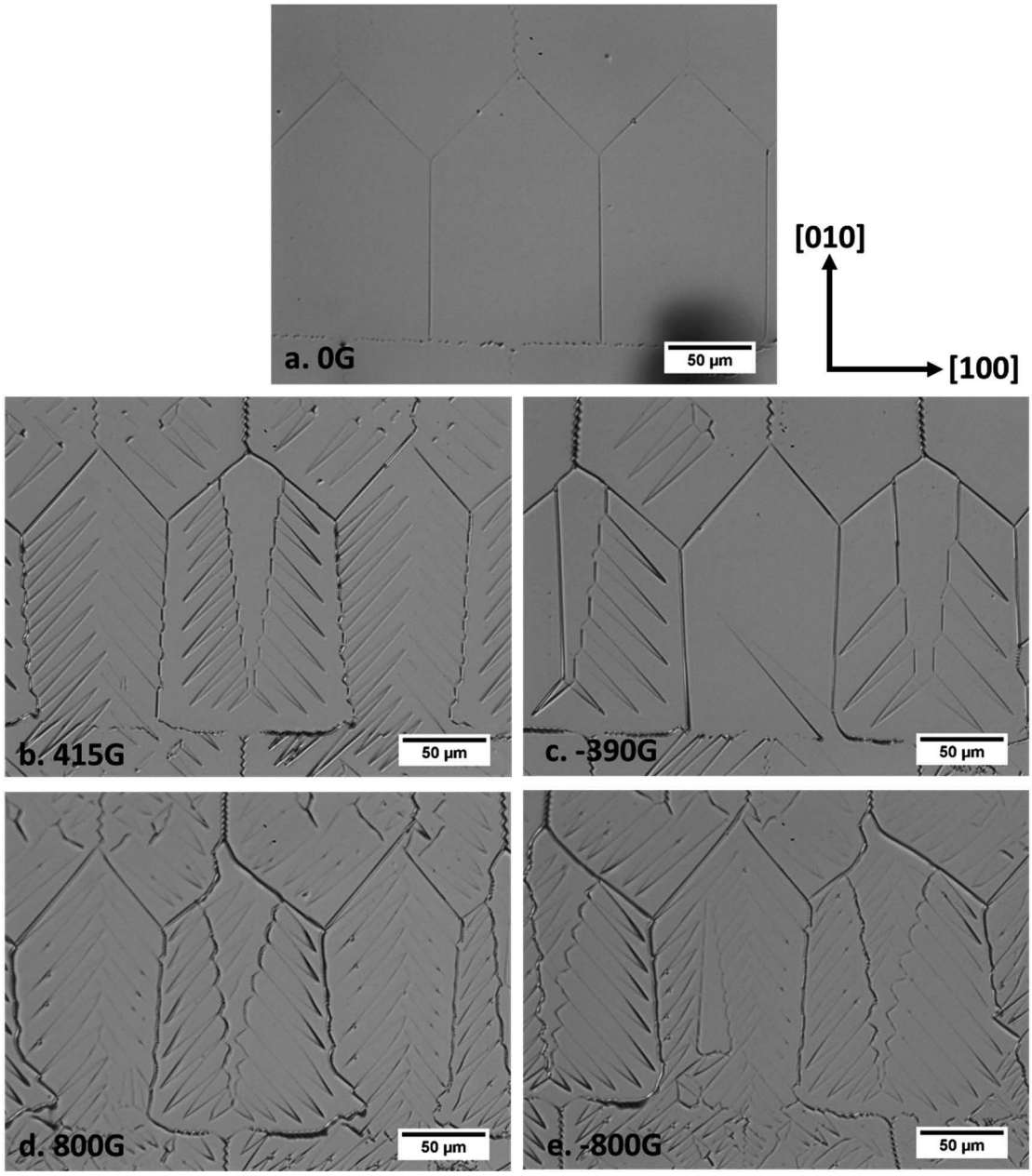

Figure 4.10: Dependence of pike domain orientation on the direction of applied magnetic field. A basic domain structure with no applied field is shown in (a). In (b) and (d) a magnetic field was applied out of the plane and in (c) and (e) a field was applied into the plane. Reversing the direction of the applied field reverses the direction of the spikes.

To test the effects of different field orientations on the formation of spike domains, the single crystal of $Fe_{91.5}Ga_{8.5}$ was subjected to large magnetic fields both out of plane and into plane. The results are summarized in Figure 4.10. The initial state is shown in Figure 4.10a, with positive magnetic fields shown in b and d, and negative magnetic fields shown in c and e. The results are consistent with expectations. When the sign of the magnetic field is reversed, the orientation of the spikes in each domain is also reversed. Since the spike and fir tree domains form with predictable orientations, they can be used to determine the true magnetization directions of any basic domain structure that they form in. For example, the magnetizations given in Figure 4.1 can be confirmed by applying a magnetic field. The spike domains in Figure 4.7 show that the analysis is consistent. The spike orientations above and below the pentagon structures are the same, confirming that these domains have the same magnetization state. This technique will be useful for analyzing other unique domain structures in this material.

4.2.3 Charged 90° domain walls

In some cases, domain walls are present but do not collect any ferrofluid. These walls are invisible under normal viewing conditions. This results in unusual structures, with domain walls that come to a stop abruptly in the middle of the material. One such pattern can be seen in Figure 4.11a. The zigzag V-lines come a stop at some points, with the domains appearing to wrap all around the domain wall. When a field is applied out of plane in Figure 4.11b half of the zigzag lines disappear. At higher fields the invisible lines begin to appear. They can be seen in Figure 4.11c and d, appearing at approximately 45° angles as would be expected for 90° domain walls. Large out-of-plane magnetic fields can be used to nucleate the spike domains seen in Figure 4.11e and f. Using the technique discussed in Section 4.2.2, the spike domains can be used to determine the domain orientations. To clarify the faint spike domains, a schematic representation is shown in Figure 4.12. Figure 4.12a represents the right side of Figure 4.11e and Figure 4.12b represents the left side of Figure 4.11f. Using Figure 4.9a-d and a knowledge of zigzag V-lines, the domain magnetization directions were established.

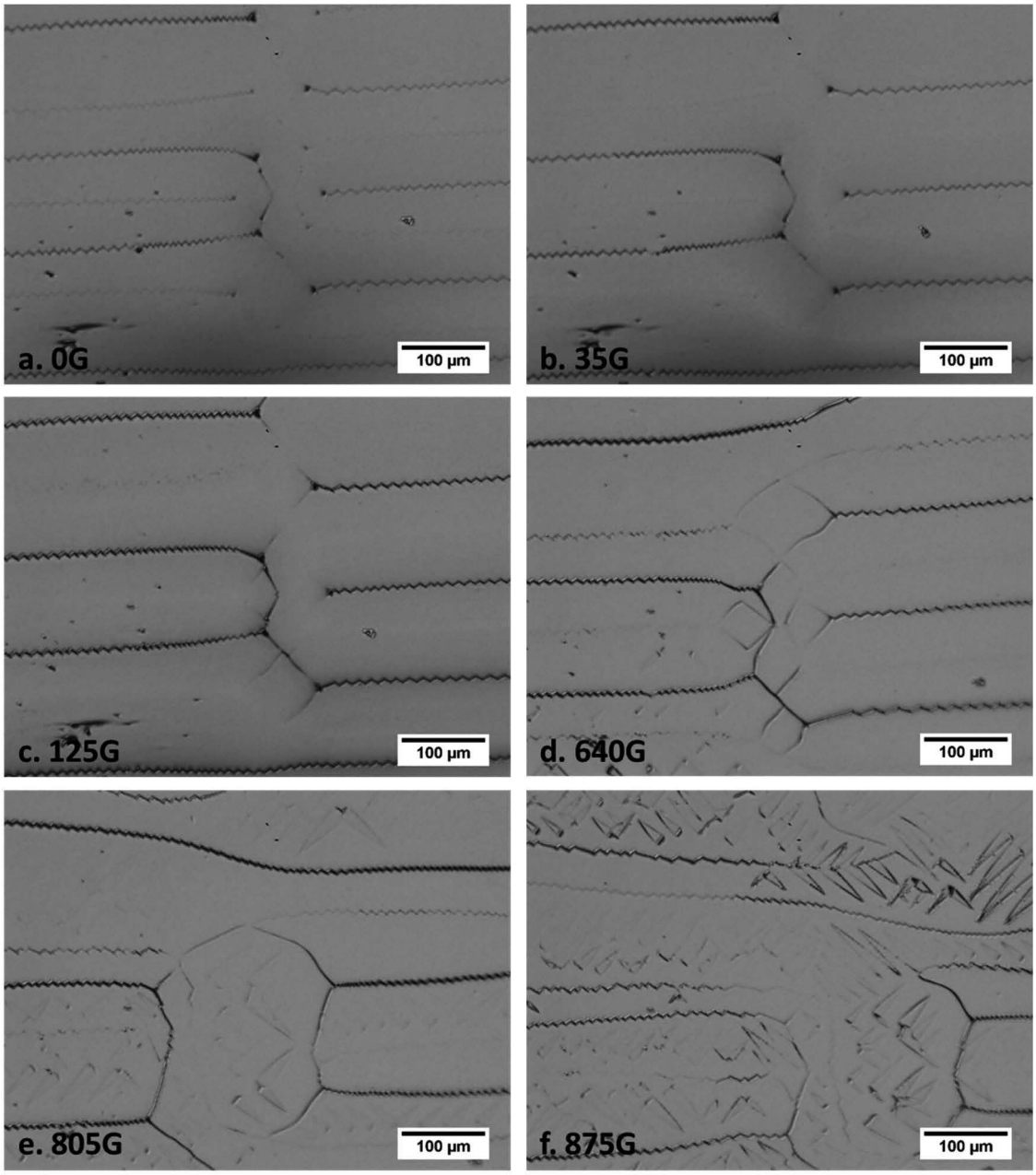

Figure 4.11: Effect of applied field on invisible domain walls. Domain patterns on (001) surface of $Fe_{91.5}Ga_{8.5}$ have some invisible domain walls (a). With increasing magnetic field applied out of plane some zigzag lines disappear (b). Invisible walls become visible in (c). More invisible walls appear in (d) and zigzag lines reappear. Spike domains form in (e) and (f) which can be used to determine domain orientation.

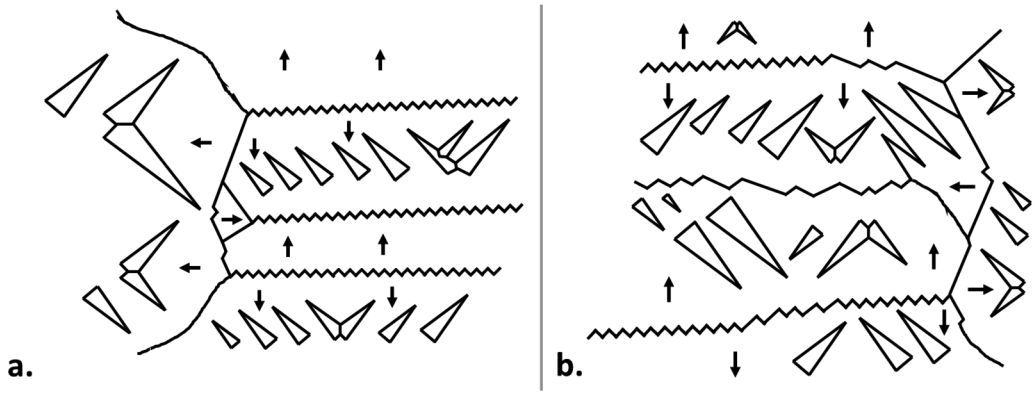

Figure 4.12: Schematics clarifying the faint domain structures in Figure 4.11e and f. The right side of Figure 4.11e is drawn in (a) and the left side of Figure 4.11f is drawn in (b). Using the orientation of the spike domains, it can be shown that the invisible domain walls were actually 90° walls with head-to-head and tail-to-tail orientations.

From this analysis it can be shown that the initially invisible domain walls are charged 90° domain walls with head-to-head and tail-to tail orientations. It is unclear why this domain orientation results in walls that do not collect ferrofluid. However, it is consistent with the observations of 90° zigzag walls where half of each zigzag tooth was faint or invisible. The faint or invisible segments (for example in Figure 4.1) were magnetically charged, with head-to-head and tail-to-tail orientations just like the invisible walls in Figure 4.11a.

The charged 90° domain walls were seen in other compositions of Fe-Ga as well. Figure 4.13a shows domains on an as-grown crystal of $Fe_{85}Ga_{15}$. A schematic representation is show in Figure 4.13c. Regular bands of zigzag V-lines are interrupted by domains enclosed by invisible charged 90° walls, with domain orientations flipped on either side of the break. In an annealed and quenched crystal of $Fe_{85}Ga_{15}$ (Figure 4.13b and d) the zigzag V-lines form a labyrinthine structure with faint or invisible 90° walls separating the corners. In general, the charged 90° walls were always associated with zigzag lines. The reason for the formation of these charged walls will be explored further in Chapter 5.

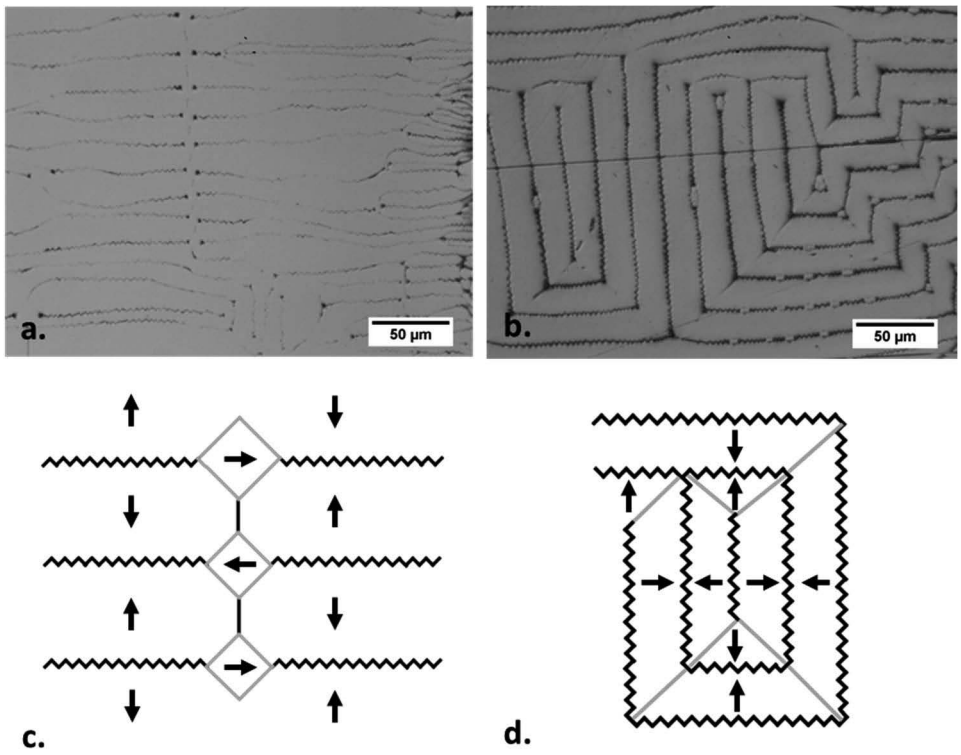

Figure 4.13: Structures with invisible domain walls. On a (001) surface of an as-grown crystal of $Fe_{85}Ga_{15}$ (a), zigzag V-lines are separated by invisible 90° walls. On a (001) surface of an annealed and quenched crystal of $Fe_{85}Ga_{15}$ (b), zigzag V-lines for a labyrinthine structure with the corners filled in by invisible or faintly visible 90° walls. The schematics in (c) and (d) show portions of (a) and (b), respectively, with their magnetizations. The faint or invisible 90° walls are shown in gray.

4.2.4 Measurements of Zigzag Lines

In Section 1.3.8 it was predicted that the thickness of the zigzag lines, defined here as twice the zigzag wave amplitude, would be proportional to the reciprocal of the magnetostrictive constant. To test this prediction, the thickness was measured for four different galfenol samples. In addition, measurements were taken from images of $Fe_{92.5}Si_{7.5}$ published by Chikazumi and Suzuki [19] and $Fe_{73.9}Ga_{26.1}$ published by Chopra and Wuttig [11]. The magnetonstrictive constant λ_{100} was determined by performing linear

interpolations on the data of Clark et al. [1] for Fe-Ga and the data of Hall [61] for Fe-Si. The results are summarized in Figure 4.14.

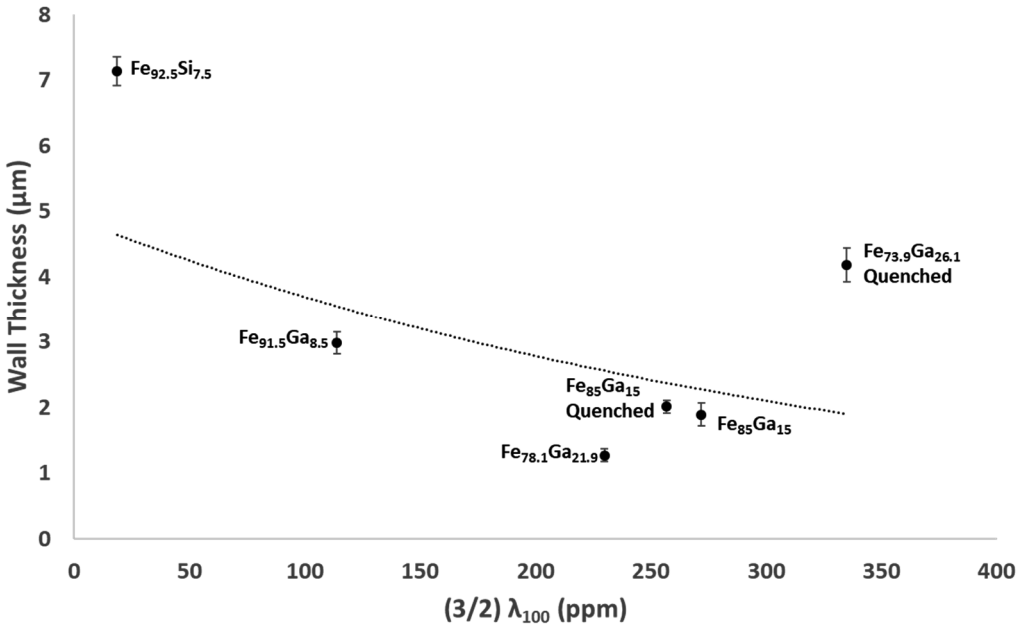

Figure 4.14: Measurements of the thickness (twice the amplitude) of zigzag lines in single crystals Fe-Ga and Fe-Si as a function of λ_{100}. For $Fe_{92.5}Si_{7.5}$ and $Fe_{73.9}Ga_{26.1}$ were taken from Chikazumi and Suzuki [19] and Chopra and Wuttig [11] respectively. The trendline shows the best fit of thickness as a function of $1/\lambda_{100}$.

The trend of thickness, t, proportional to $1/\lambda_{100}$ does not fit the data. There could be a few reasons for this discrepancy. First, λ_{100} is not the only property that influences the thickness. It is also influenced by the anisotropy and exchange constants (which affect the zigzag angle, ω, and the gradient energy constant, β) so that materials containing different phases will exhibit different behavior. Also, surface stresses may be induced by quenching (as will be discussed more later) which could influence the magnetoelastic energy which controls the thickness.

4.3 Conclusions

A variety of magnetically charged domain structures were explored here. A pentagonal domain structure, never before see in galfenol, was described for the first time here. Two methods of determining the magnetization of basic domain structures by the application of out-of-plane fields were described and formalized. One used the alternating disappearance of zigzag lines. The other utilized the orientation of spike and fir tree domains. Both methods were combined to show that the pentagonal domain structures contained a new type of zigzag wall, a charged 90° zigzag wall, which is unlike the familiar zigzag V-lines. The spike domains were also used to demonstrate that invisible or faintly visible domain walls were charged 90° domain walls with head-to-head and tail-to-tail orientations.

5 Chain Domains

5.1 Introduction

The tools developed in Chapter 4 will be helpful in analyzing the magnetization state of the chain (cellular) domain structure. In this chapter, a new interpretation of the chain domain structure will be presented. Chain domains in galfenol are compared with similar structures in Fe-Si alloys to help understand the role of elasticity in their formation.

5.2 Results and Discussion

Interesting domain structures were found on an annealed and quenched single crystal of $Fe_{85}Ga_{15}$. Zigzag V-lines come together to form regular chains of rectangular units (Figure 5.1). Inside of each rectangular unit there is a fifth zigzag line running parallel to the long axis but not touching the edges of the rectangle. It is assumed that the centerline connects to the corners of each unit by unseen charged 90° walls, much like the rectangular shape in the center of Figure 4.13d. Domains of this form were previously reported by Chopra [11], who referred to them as cellular domains. In this work they will be referred to as chain domains.

The chain structure does not always form rectangles with square corners. Figure 5.2 shows how the chain domains can vary. They can be somewhat rounded and they can be very rounded, narrowing to a point on the end. In transitionary structures like at the top of the figure, the individual units grow out from a zigzag V-line, forming a structure like a beaded string. These “beads” can be very small, like those seen in Figure 4.13b.

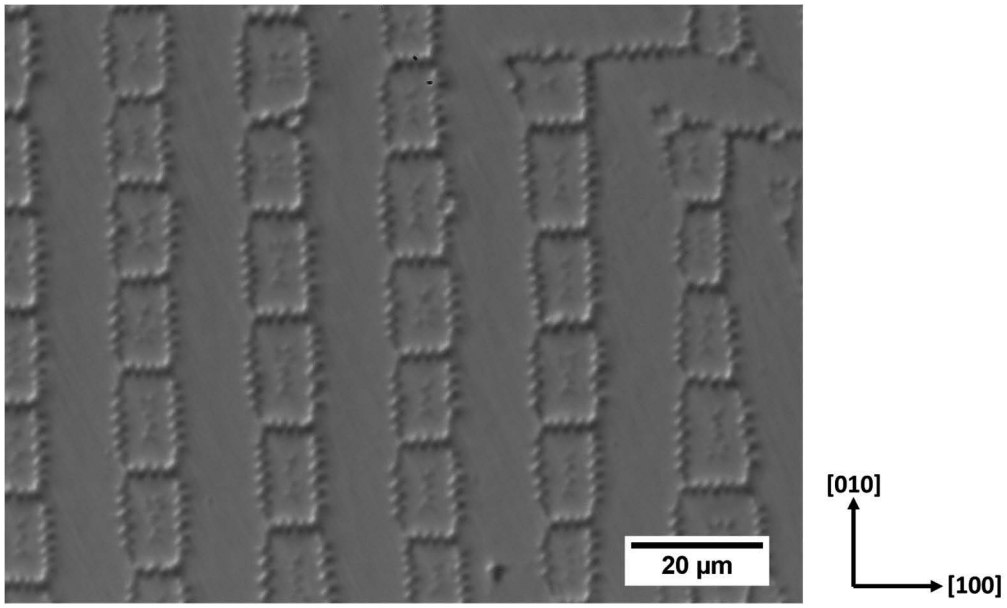

Figure 5.1: Chain-like domain structure seen on (001) surface of annealed and quenched single crystal of $Fe_{85}Ga_{15}$. The borders of each chain link and the line through the center are zigzag V-lines. Charged 90°domain walls connect to centerline to the corners.

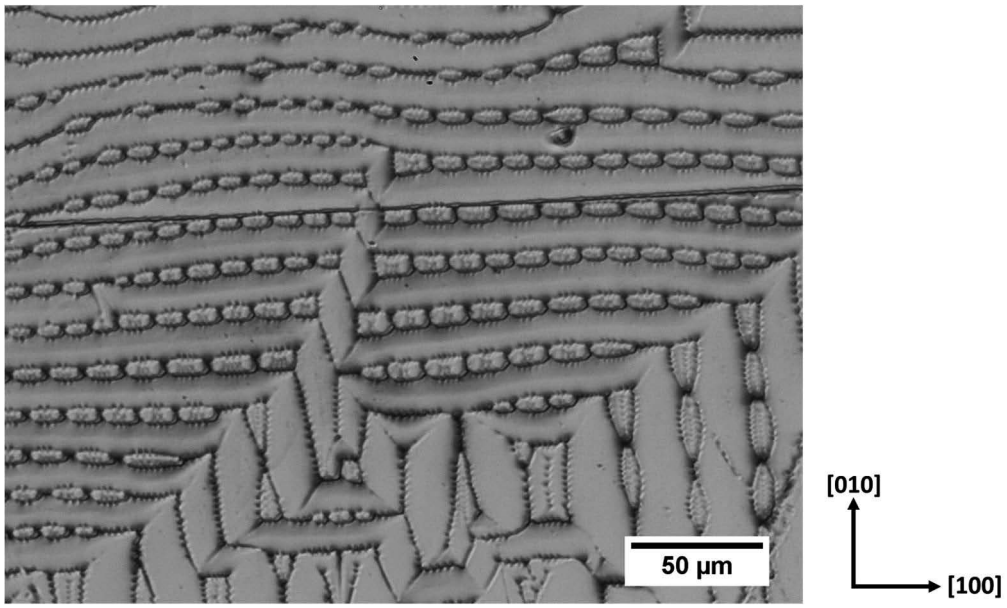

Figure 5.2: Variable chain domain structure seen on (001) surface of annealed and quenched single crystal of $Fe_{85}Ga_{15}$. The shape of the chains can vary, with chains of square links, chains of rounded links, or beaded string structures with the domains growing from zigzag V-lines.

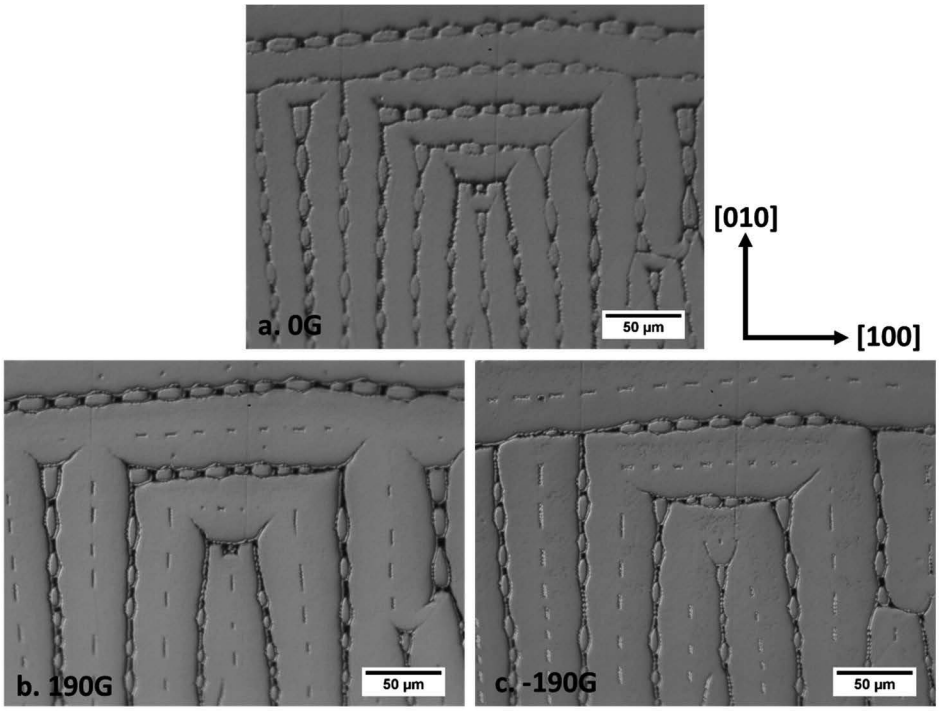

Figure 5.3: Effects of applied field on chain domains. Chains domains were seen on the (001) surface of an annealed and quenched single crystal of $Fe_{85}Ga_{15}$ (a). When an out-of-plane field was applied (b) the outer edges of some chain links disappeared and the centerline of neighboring chains disappeared. In a reversed field (c) the alternating pattern is reversed.

To clarify the magnetization directions within the chains, a magnetic field was applied perpendicular to the surface. The initial state is shown in Figure 5.3a. Figure 5.3b and c show positive and negative fields, respectively. Under an applied field the outer walls of every other chain disappear, leaving only the centerline visible. In the neighboring chains this behavior is reversed, with the centerline disappearing and the outer walls remaining visible. This indicates that all of the zigzag lines forming the boundaries of the chain links have the same orientation. They either all point inwards or all point outwards, with the centerline having the opposite orientation. This is illustrated in Figure 5.4. The convergence of so many V-lines in a narrow area creates a complex three-dimensional geometry beneath the surface. A three-dimensional model of the chain domains is given in Figure 5.5. For simplicity, the zigzag folding of the 90° domain walls is ignored in this

model. Each chain link results from a subsurface domain magnetized perpendicular to the surface, represented as rectangles in Figure 5.5b. This magnetization meets the surface at the centerline of the chain link and then spreads out in four directions.

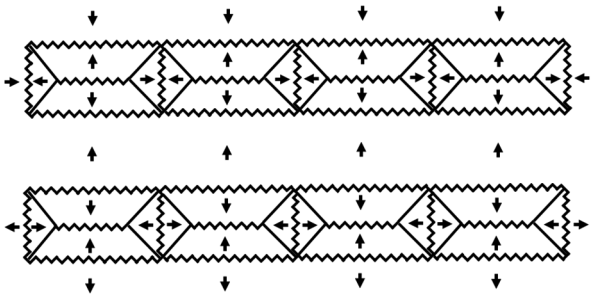

Figure 5.4: Magnetization state of chain domains. Alternating chains have opposite orientations.

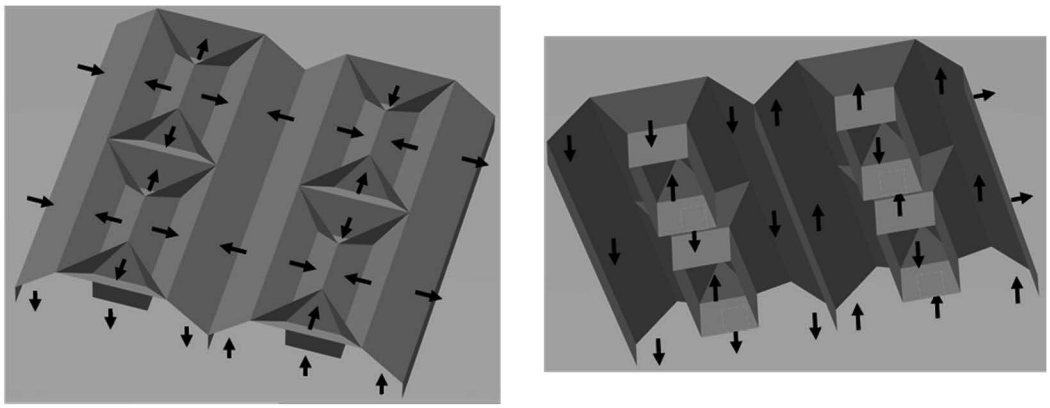

Figure 5.5: Three-dimensional model of the chain domain structure as viewed from above (a) and below (b).

In general, the subsurface domains forming these chain links are not expected to penetrate deep into the bulk. The domain wall energy can be reduced by a branched structure, with many small domains near the surface coming together to form larger domains within the bulk. Evidence of domain branching was seen on a single crystal of $Fe_{83}Ga_{17}$, shown in Figure 5.6. Near the free surface on the left side there are many small domain branches. Deep in the material these branches merge together to form coarse domain structures to reduce domain wall energy.

Figure 5.6: Evidence of domain branching on a (001) surface of $Fe_{83}Ga_{17}$. Domains are fine near the free surface, but become coarse at large depths. The thick vertical line at the left of the image is a scratch.

It can be shown that the magnetoelastic energy is reduced by splitting into four domains instead of two. This requires considering a component of the elasticity that was previously ignored. Figure 5.7a shows a cross section through two zigzag lines in an imaginary strain free state. The zigzag folded 90° walls have an elastic energy component caused by the strain mismatch on the domain wall. The extra component of elastic energy results from geometric incompatibility. In Figure 5.7b, the domains are isolated from each other and allowed to experience strain from magnetostriction. After elongating along the magnetization direction, the domains no longer fit together. Since the domains are forced to fit together, a compressive stress is generated as a result of the incompatibility.

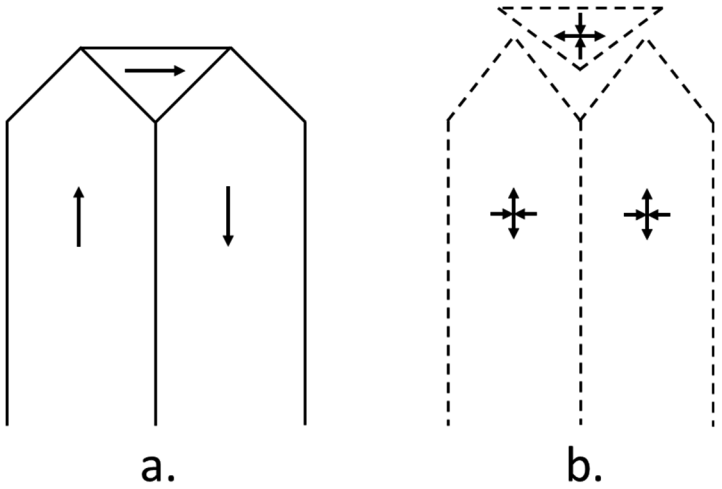

Figure 5.7: Strain state zigzag domain wall structures. In (a) the unstrained state is shown with the magnetization vectors. The strained state is shown in (b) where the arrows represent the magnetostrictive strain. There is a stress caused by the shape incompatibility.

A periodic arrangement like the chain structure can help to mitigate the stress caused by strain mismatch. To understand this, consider the cross section of the chain domains in Figure 5.8. On the (100) cross section in Figure 5.8a, the long primary surface domains can be seen. These domains apply a compressive stress on the underlying domains along the [010] axis. The (010) cross section in Figure 5.8b shows the effect of the secondary triangular domains. These secondary domains exert a stress on the [100] axis, but contract along the [010] axis. This contraction counteracts some of the stress induced by the primary domains. By alternating magnetization axes in a periodic arrangement, the average stress can be reduced. This provides a potential driving force for the preference towards long range ordering in the domain structure.

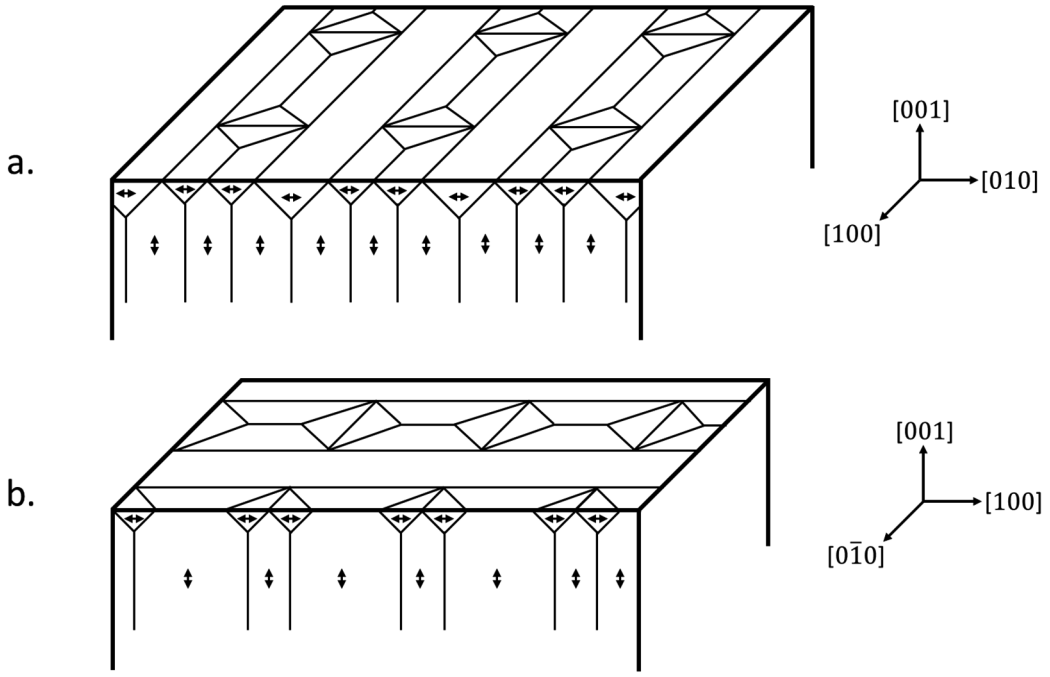

Figure 5.8: Reduction of magnetoealastic energy in chain domains. Zigzag lines are drawn straight for simplicity. The long primary domains (a) exert a compressive stress on the subsurface domains on the [010] axis. The secondary triangular domains exert a stress on the [100] axis. The associated contraction of the secondary domains on the [010] axis relieves some stress.

The variation in chain domain structure must also be considered. A few of the possible chain structures are given in Figure 5.9.The chains can be square or rounded to a narrow tip. Some chains branch to form smaller chains, and some can even form small chains on the walls of larger chains to create a nested structure. Different shapes must be interpreted somewhat differently. For example, the beaded string geometry seen at the top of Figure 5.2. These domains narrow all the way to a point, leaving no space for 90° domain walls at the end. These structures contain only two domains instead of the typical four. This is illustrated in Figure 5.10. The links with curved walls are intermediate structures. The narrowing of the boundaries results in smaller domains on the ends.

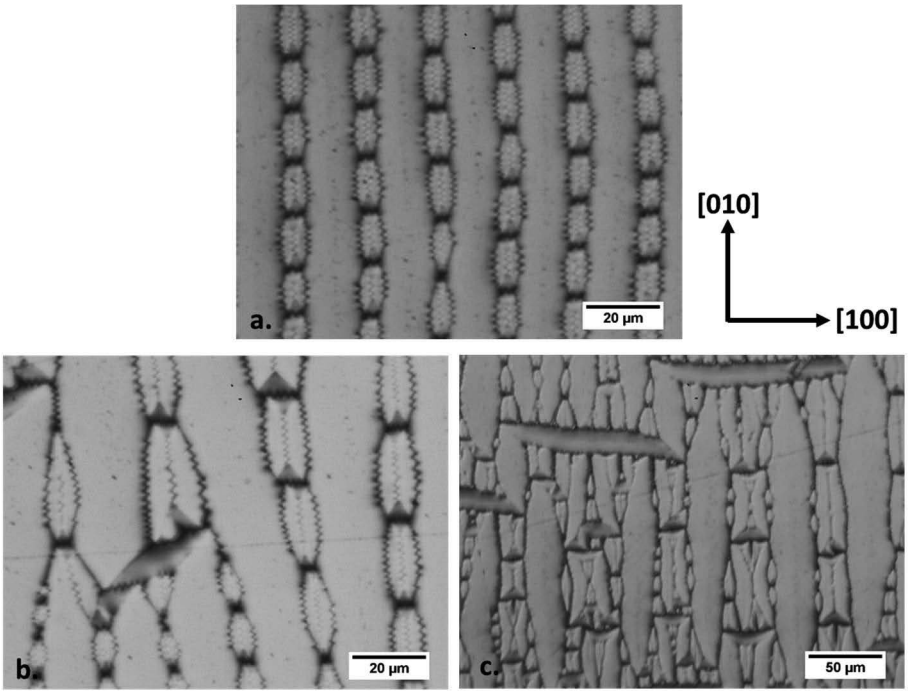

Figure 5.9: Examples of variation in chain domains on (001) surface of annealed and quenched single crystal of $Fe_{85}Ga_{15}$. Domain can form regular parallel chains (a), they can be rounded to a narrow point and split into smaller chains (b), and the form nested structures with chains on chains (c).

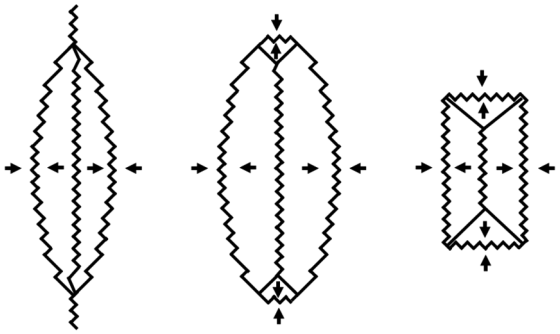

Figure 5.10: Different chain domain geometries. Chain links that narrow to a point have only two internal domains instead of four.

5.3 Comparison Between Domain Structures in Fe-Ga and Fe-Si

Despite large differences in magnetoelastic properties, Fe-Si alloys have many interesting structures that are analogous to structures in galfenol. This includes some structures of interest in this work, like zigzag V-lines and chain domains. For this reason, it is worth comparing and contrasting the structures seen in both alloys and the mechanisms that are responsible for their formation.

The so-called cellular structure observed by Chopra in galfenol [11, 54] is fascinating, but not the first observation of such structures. Carey [62] observed a so-called band structure in (100) textured sheets of Fe-Si (unknown composition). The structure consisted of a series of parallel zigzag lines, but the same term was used to refer to chain-like structures of rectangular links. The author appears not to have recognized the significance of this difference, and did not comment on it. They supposed that the structure was a result of residual compressive stressed from rolling which caused a preference for out of plane magnetization. The addition of a tensile stress in the plane caused this structure to disappear.

Chikazumi and Suzuki [46] created compressive surface stresses in a single crystal with 4 wt%Si by dropping a ball-point pen on a (100) surface. They polished the indent completely off and observed what they called chain-like domains in the area of the indent. The image is once again not of sufficient quality to resolve internal structure, but they are chain-like in appearance.

The most significant work on chain domains was done by Stephan, who took high quality images of these structures on a (100) surface of a quenched Fe-Si single crystal [63]. Like the domains seen in galfenol, the chain links had four zigzag edges and a fifth zigzag line running through the center. It also contained charged head-to-head and tail-to-tail 90° domain walls, which were invisible to the ferrofluid. Stephan determined the domain orientations in the same way as for galfenol, by applying an out-of-plane field and

noting that the centerlines disappeared in every other chain while the outer edges disappeared in the other chains.

Stephan attributed the formation of the chain structure to residual compressive stresses caused by the quenching of the crystal. The severity of the quenching altered the form of the chains [64]. More aggressive quenching resulted in nested chain structures, with chains growing from the walls of other chain links. When these were subjected to a tensile stress, the complexity of the structure was reduced. Starting with a nested chain structure, increases in stress caused the secondary chain links to disappear. Then the square links became round and lost the triangular secondary domains at their ends. With sufficient applied stress, the compressive stresses were removed and the chain structure disappeared. Stephan had a good grasp on the interpretation of the chain structure, but could not explain what role the elasticity played in the formation of secondary triangular domains in the cells.

The periodic structure of the chain domains and their intimate relationship with stress can leave no doubt their formation is driven by elasticity. Like the simpler zigzag domain structures, a compressive stress will favor domain orientations perpendicular to the surface. This naturally promotes any structure containing V-lines at the surface. Indeed, whenever chain domains have been seen on a (100) surface of Fe-Si, some form of compressive plane stress was present.

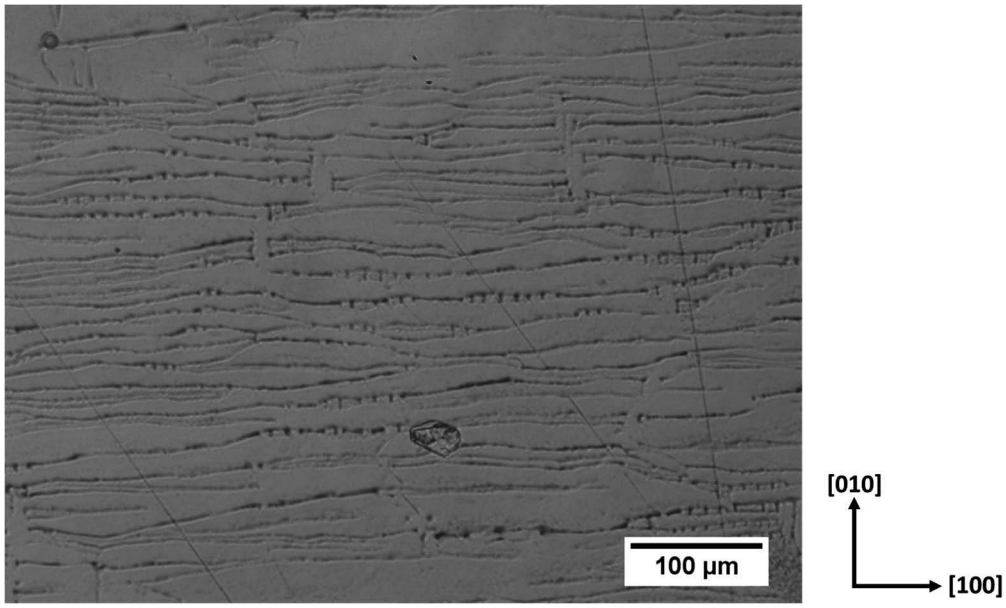

Figure 5.11: Chain domains on (100) surface of as-grown crystal of $Fe_{82.9}Ga_{17.1}$.

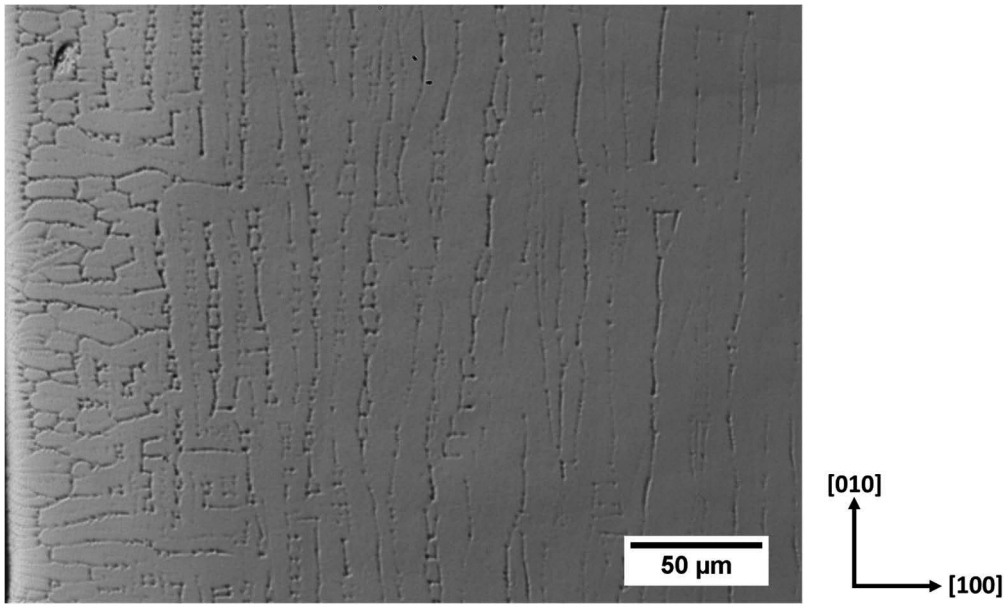

Figure 5.12: Chain domains on (100) surface of as-grown crystal of $Fe_{78.1}Ga_{21.9}$.

The influence of quenching-induced surface stress may play some part in the observation of chain domains in galfenol as well. The chain domains shown in Chapter 5 were from a quenched crystal of $Fe_{85}Ga_{15}$. However, chain domains were also observed on as-grown crystals of $Fe_{82.9}Ga_{17.1}$ (Figure 5.11) and $Fe_{78.1}Ga_{21.9}$ (Figure 5.12). Chopra et al.

also observed complex chain domain structures on slow cooled crystals of $Fe_{73.9}Ga_{26.1}$. It appears that surface stresses from quenching are capable of producing chain domain structures, but they are not necessary in galfenol where they are seen on stress-free surfaces of unquenched samples.

The reason stress is needed to form chain domains in Fe-Si stems from the difference in magnetostriction as compared with galfenol. In general, additions of Ga increase magnetostriction in Fe, while additions of Si decrease magnetostriction.This effect is summarized in Figure 5.13, a plot of $\frac{3}{2}\lambda_{100}$ vs. composition for Fe-Ga and Fe-Si. Magnetostriction data was taken from Clark et al. [1] and Hall [61].

Structures with regularly spaced zigzag lines have been seen in stress-free crystals of both galfenol (e.g. Figure 4.1) and Fe-Si [47]. The driving force for the transition from simple zigzag lines to a chain structures is a reduction in magnetoelastic energy. This reduction must be great enough to overcome the additional domain wall energy. The reduction in magnetoelastic energy becomes greater with increasing magnetostriction, while the energy cost remains constant. For a highly magnetostrictive alloy like galfenol, the energy reductions caused by the formation of the chain structure outweigh the costs. This is not the case for Fe-Si, which has an order of magnitude less magnetostriction. For low magnetostrictive Fe-Si alloys, the addition of compressive residual stresses must provide some additional driving force for the formation of chain domains.

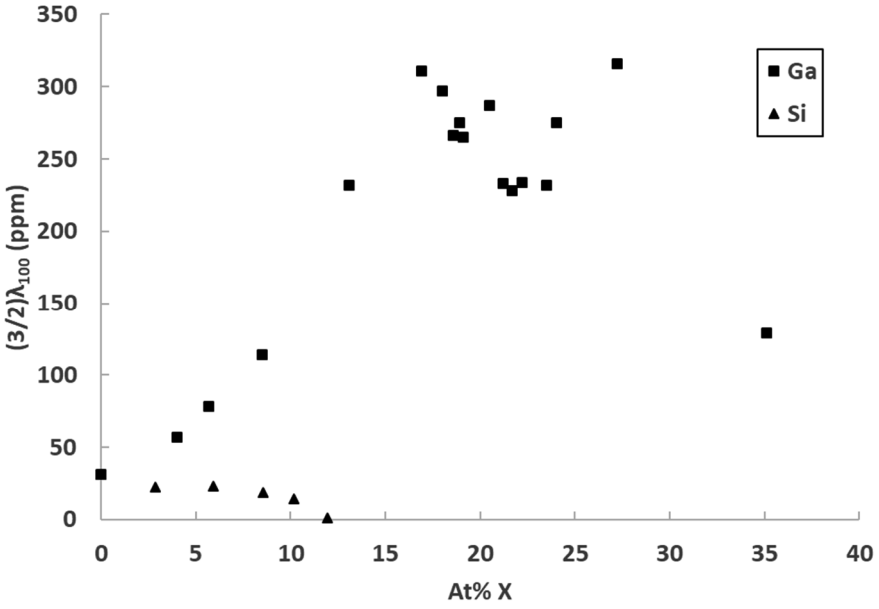

Figure 5.13: Plot of $\frac{3}{2}\lambda_{100}$ vs. at% Ga and at% Si in Fe. Adding Ga causes a strong increase in magnetostriction, while adding Si decreases magnetostriction.

5.4 Conclusions

The chain domain structure, first described in galfenol by Chopra and Wuttig [11], was thoroughly characterized and reevaluated. The response of zigzag lines to out-of-plane fields was used to determine the magnetization state of the chains, which differed from the interpretation presented by Chopra and Wuttig. The chains can be seen as a more complex version of zigzag lines. The zigzag V-lines form to ensure flux closure and minimize the magnetostatic energy. The chain structure forms to reduced the magnetoelastic energy created by the geometric incompatibility of strains in the surface domains. For highly magnetostrictive materials, the magnetostatic energy incurred by the formations charged 90° domain walls is offset by a reduction in magnetoelastic energy afforded by the alternation of surface domain orientations. These chain domains can form in both quenched and slow cooled crystals, so they cannot be explained by the influence of quench induced compressive surface stresses alone.

6 Summary of Conclusions

Galfenol has drawn a great deal of interest because of its attractive combination of properties, including large magnetostriction of up to 400 ppm and good ductility and machineability. Despite this interest, little characterization has been done on the true domains structures in this promising material. The domain studies that have been performed generally only consider one composition and one domain structure. Of these, many only show maze domain structures of zigzag walls which are caused by polishing induced surface stresses, and do not represent the true domain structure. Removing this stress by careful surface preparation, a few authors have reported on simple closure domain structure. Finally, a few works reported on a cellular or chain domain structure. A more comprehensive study was necessary to more fully explore the possible magnetic domain structure in galfenol and to better explain the poorly understood chain domain structure.

In this work, several new domain structures are presented which were never seen before in galfenol, and methods were developed for the interpretation of these domain structures. A magnetic field applied perpendicular to the surface can be used to determine the relative orientation of zigzag V-lines, which preferentially disappear in Bitter images depending on the magnetization of surrounding domains. Stronger fields can be used to induce spike and fir tree domains, whose orientation is uniquely defined by the magnetization of the parent domains and the direction of the applied fields.

A new pentagonal arrangement of domain walls was described in galfenol. This structure was periodic over long distances and contained a new type of zigzag domain wall. These 90° charged zigzag walls have not been described in galfenol previously. Applied fields were also used to demonstrate the existence of 90° walls with head-to-head and tail-to-tail orientations.

Through a thorough investigation of domain phenomena physically meaningful and self-consistent interpretation of the chain domains was developed. The magnetization points either outward in all four domains or inward in all four domains. Each chain link

contains five zigzag V-lines and four charged 90° walls. The secondary triangular domains at the end of each chain link help to reduced the magnetoelastic energy by distributing stresses along two different axes. This interpretation provides a better explanation for the zigzag walls and provides a simpler mechanism for the elastic interactions, without resorting to magnetizations which deviate from the easy axes, as other authors have done.

7 Future Work

In this work, only domain structures on the (100) plane were considered, but another class of domain structures exist on (110) surfaces of galfenol. These structures have been characterized to a small extent but were not included here. Figure 7.1 shows an example of a domain structure on a (110) surface of $Fe_{89.3}Ga_{10.7}$. These structures are difficult to analyze because there is only one easy direction in the plane of the sample. More work needs to be done to understand these complex structures. Some of the walls appear chain-like, but since they occur on a (110) plane the mechanisms for their formation must be different. Similar structures have also been observed in Fe-Si by Corner and Mason [65], Bates and Hart [66], and Stephan [64].

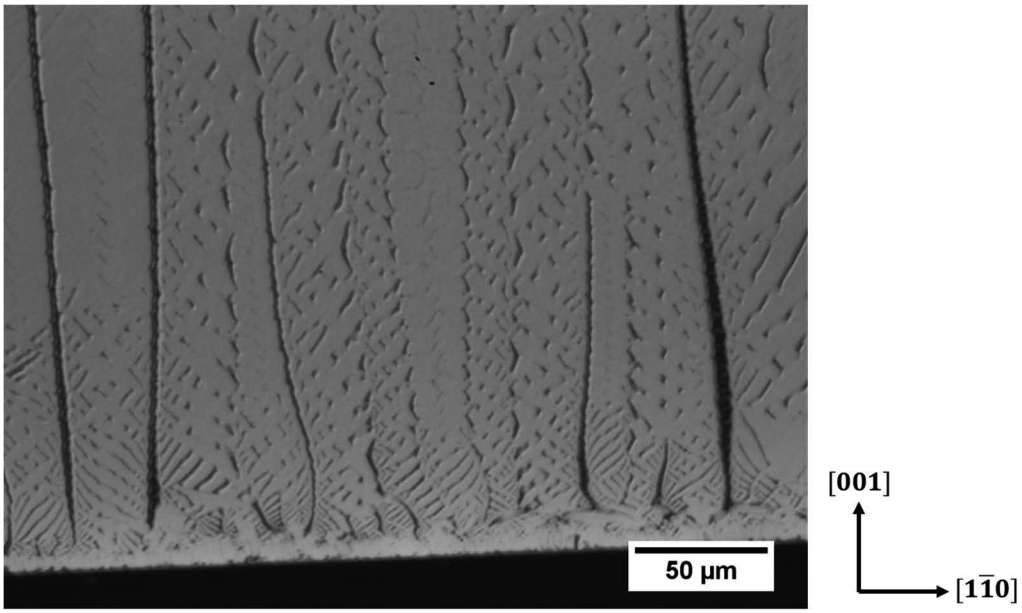

Figure 7.1: Domain structure on a (110) surface of $Fe_{89.3}Ga_{10.7}$.

8 Reference List

[1] A. Clark *et al.*, "Extraordinary magnetoelasticity and lattice softening in bcc Fe-Ga alloys," *Ames Laboratory Conference Papers, Posters, and Presentations,* 2003.

[2] R. A. Kellogg, A. M. Russell, T. A. Lograsso, A. B. Flatau, A. E. Clark, and M. Wun-Fogle, "Mechanical properties of magnetostrictive iron-gallium alloys," 2003, vol. 5053, pp. 534-543.

[3] E. M. Summers, T. A. Lograsso, J. D. Snodgrass, and J. C. Slaughter, "Magnetic and mechanical properties of polycrystalline Galfenol," 2004, vol. 5387, pp. 448-459.

[4] J. Ellison, J. Sirohi, and I. Chopra, "Investigation of active materials as driving elements of a hydraulic hybrid actuator," 2005, vol. 5764, pp. 274-289.

[5] Z. G. Zhang, T. Ueno, T. Yamazaki, and T. Higuchi, "Primary Analysis of Frequency Characteristics in a Miniature Self-Propelling Device Using Fe-Ga Alloys (Galfenol)," *IEEE Transactions on Magnetics,* vol. 46, no. 6, pp. 1641-1644, 2010.

[6] T. Ueno and T. Higuchi, "Investigation of Micro Bending Actuator using Iron-Gallium Alloy (Galfenol)," in *2007 International Symposium on Micro-NanoMechatronics and Human Science*, 2007, pp. 460-465.

[7] T. Ueno and T. Higuchi, "Two-DOF Micro Magnetostrictive Bending Actuator for Wobbling Motion," *IEEE Transactions on Magnetics,* vol. 44, no. 11, pp. 4078-4080, 2008.

[8] M. Ghodsi, T. Ueno, H. Teshima, H. Hirano, T. Higuchi, and E. Summers, ""“Zero-power” positioning actuator for cryogenic environments by combining magnetostrictive bimetal and HTS," *Sensors and Actuators A: Physical,* vol. 135, no. 2, pp. 787-791, 2007.

[9] T. Ueno, E. Summers, M. Wun-Fogle, and T. Higuchi, "Micro-magnetostrictive vibrator using iron–gallium alloy," *Sensors and Actuators A: Physical,* vol. 148, no. 1, pp. 280-284, 2008.

[10] V. Berbyuk, "Vibration energy harvesting using Galfenol-based transducer," 2013, vol. 8688, pp. 86881F-86881F-12.

[11] H. D. Chopra and M. Wuttig, "Non-Joulian magnetostriction," *Nature,* vol. 521, p. 340, 2015.

[12] S. Rafique, J. R. Cullen, M. Wuttig, and J. Cui, "Magnetic anisotropy of FeGa alloys," vol. 95, no. 11, pp. 6939-6941, 2004.

[13] J. B. Restorff, M. Wun-Fogle, A. E. Clark, and K. B. Hathaway, "Induced Magnetic Anisotropy in Stress-Annealed Galfenol Alloys," *IEEE Transactions on Magnetics,* vol. 42, no. 10, pp. 3087-3089, 2006.

[14] Y. Jin, "Theory, modeling, and simulation of structural and functional materials: Micromechanics, microstructures, and properties," Rutgers University, New Brunswick, NJ, 2003.

[15] A. G. Khachaturyan, *Theory of Structural Transformations in Solids*. Dover Publications, 2013, p. 594.

[16] L. Landau and E. Lifshits, "On the Theory of the Dispersion of Magnetic Permeability in Magnetic Bodies," *Physikalische zeitschrift der Sowjetunion,* vol. 8, pp. 153-169, 1935.

[17] A. Hubert and R. Schafer, *Magnetic Domains: The Analysis of Magnetic Microstructures*. Berlin, Germany: Springer, 1998.

[18] B. A. Lilley, "LXXI. Energies and widths of domain boundaries in ferromagnetics," *The London, Edinburgh, and Dublin Philosophical Magazine and Journal of Science,* vol. 41, no. 319, pp. 792-813, 1950.

[19] S. Chikazumi and K. Suzuki, "On the Maze Domain of Silicon-Iron Crystal (I)," *Journal of the Physical Society of Japan,* vol. 10, no. 7, pp. 523-534, 1955.

[20] O. Ikeda, R. Kainuma, I. Ohnuma, K. Fukamichi, and K. Ishida, "Phase equilibria and stability of ordered b.c.c. phases in the Fe-rich portion of the Fe–Ga system," *Journal of Alloys and Compounds,* vol. 347, no. 1–2, pp. 198-205, 2002.

[21] T. A. Lograsso and E. M. Summers, "Detection and quantification of D03 chemical order in Fe–Ga alloys using high resolution X-ray diffraction," *Materials Science and Engineering: A,* vol. 416, no. 1, pp. 240-245, 2006.

[22] H. Okamoto, *Phase diagrams of binary iron alloys*. Materials Park, OH: ASM International, 1993.

[23] N. Kawamiya, K. Adachi, and Y. Nakamura, "Magnetic Properties and Mössabauer Investigations of Fe-Ga Alloys," *Journal of the Physical Society of Japan,* vol. 33, no. 5, pp. 1318-1327, 1972.

[24] H. Wagini, "Magnetische, elektrische und thermische Eigenschaften der bcc-a-Phase im System Fe—Ga," *Zeitschrift fur Naturforschung - Section A Journal of Physical Sciences,* Article vol. 22, no. 1, pp. 143-144, 1967.

[25] Q. Xing, Y. Du, R. J. McQueeney, and T. A. Lograsso, "Structural investigations of Fe–Ga alloys: Phase relations and magnetostrictive behavior," *Acta Materialia,* vol. 56, no. 16, pp. 4536-4546, 2008.

[26] J. R. Cullen, A. E. Clark, M. Wun-Fogle, J. B. Restorff, and T. A. Lograsso, "Magnetoelasticity of Fe–Ga and Fe–Al alloys," *Journal of Magnetism and Magnetic Materials,* vol. 226, pp. 948-949, 2001.

[27] R. Wu, Z. Yang, and J. Hong, "First-principles determination of magnetic properties," (in en), *J. Phys.: Condens. Matter,* vol. 15, no. 5, p. S587, 2003.

[28] C. Paduani and C. Bormio-Nunes, "Density functional theory study of Fe3Ga," *Journal of Applied Physics,* vol. 109, no. 3, p. 033705, 2011.

[29] S. Pascarelli, M. P. Ruffoni, R. S. Turtelli, F. Kubel, and R. Grössinger, "Local structure in magnetostrictive melt-spun Fe80Ga20 alloys," *Phys. Rev. B,* vol. 77, no. 18, p. 184406, 2008.

[30] H. Wang, Z. D. Zhang, R. Q. Wu, and L. Z. Sun, "Large-scale first-principles determination of anisotropic mechanical properties of magnetostrictive Fe–Ga alloys," *Acta Materialia,* vol. 61, no. 8, pp. 2919-2925, 2013.

[31] A. G. Khachaturyan and D. Viehland, "Structurally Heterogeneous Model of Extrinsic Magnetostriction for Fe-Ga and Similar Magnetic Alloys: Part I. Decomposition and Confined Displacive Transformation," (in en), *Metall and Mat Trans A,* vol. 38, no. 13, pp. 2308-2316, 2007.

[32] A. G. Khachaturyan and D. Viehland, "Structurally Heterogeneous Model of Extrinsic Magnetostriction for Fe-Ga and Similar Magnetic Alloys: Part II. Giant Magnetostriction and Elastic Softening," (in en), *Metall and Mat Trans A,* vol. 38, no. 13, pp. 2317-2328, 2007.

[33] F. Bai, H. Zhang, J. Li, and D. Viehland, "Magnetic force microscopy investigation of the static magnetic domain structure and domain rotation in Fe-x at. %Ga alloys," *Appl. Phys. Lett.,* vol. 95, no. 15, p. 152511, 2009.

[34] F. Bai, J. Li, D. Viehland, D. Wu, and T. A. Lograsso, "Magnetic force microscopy investigation of domain structures in Fe–xat.% Ga single crystals (12<x<25)," *Journal of Applied Physics,* vol. 98, no. 2, p. 023904, 2005.

[35] J. K. Zhou, D. D. Li, and J. G. Li, "Magnetic force microscopy observation of undercooled Fe 81 Ga 19 magnetostrictive alloys," (in en), *J. Phys. D: Appl. Phys.,* vol. 41, no. 20, p. 205405, 2008.

[36] J. Zhang, T. Ma, and M. Yan, "Magnetic force microscopy study of heat-treated Fe81Ga19 with different cooling rates," *Physica B: Condensed Matter,* vol. 405, no. 15, pp. 3129-3134, 2010.

[37] A. A. Emdadi, S. H. Nedjad, and H. B. Ghavifekr, "Effect of Solidification Texture on the Magnetostrictive Behavior of Galfenol," (in en), *Metall and Mat Trans A,* vol. 45, no. 2, pp. 906-910, 2014.

[38] H. Z. Song *et al.*, "Influence of stress on the magnetic domain structure in Fe81Ga19 alloys," *Journal of Applied Physics,* vol. 105, no. 1, p. 013913, 2009.

[39] M. Barturen *et al.*, "Crossover to striped magnetic domains in Fe1−xGax magnetostrictive thin films," *Appl. Phys. Lett.,* vol. 101, no. 9, p. 092404, 2012.

[40] A. Emdadi, "Microstructure of polycrystalline Fe82Ga18 sample with solidification texture," *Rare Metals,* vol. 35, no. 9, pp. 686-690, 2016.

[41] A. A. Emdadi, J. Cifre, O. Y. Dementeva, and I. S. Golovin, "Effect of heat treatment on ordering and functional properties of the Fe–19Ga alloy," *Journal of Alloys and Compounds,* vol. 619, pp. 58-65, 2015.

[42] V. V. Palacheva *et al.*, "Phase transitions as a tool for tailoring magnetostriction in intrinsic Fe-Ga composites," *Acta Materialia,* vol. 130, pp. 229-239, 2017.

[43] S. Wen, Y. Ma, D. Wang, Z. Xu, S. Awaji, and K. Watanabe, "Magnetostriction enhancement by high magnetic field annealing in cast Fe81Ga19 alloy," *Journal of Magnetism and Magnetic Materials,* vol. 442, pp. 128-135, 2017.

[44] X. Li, X. Bao, Y. Liu, L. Yu, J. Li, and X. Gao, "Tailoring magnetostriction with various directions for directional solidification Fe82Ga15Al3 alloy by magnetic field heat treatment," *Appl. Phys. Lett.,* vol. 111, no. 16, p. 162402, 2017.

[45] C. Mudivarthi, S.-M. Na, R. Schaefer, M. Laver, M. Wuttig, and A. B. Flatau, "Magnetic domain observations in Fe–Ga alloys," *Journal of Magnetism and Magnetic Materials,* vol. 322, no. 14, pp. 2023-2026, 2010.

[46] S. Chikazumi and K. Suzuki, "On maze domains in silicon iron crystal," *IEEE Transactions on Magnetics,* vol. 15, no. 5, pp. 1291-1295, 1979.

[47] L. F. Bates and R. Carey, "Domain Patterns on ` Cube-textured ' Silicon-Iron Sheet," *Proceedings of the Physical Society,* vol. 76, no. 5, pp. 754-758, 1960.

[48] S. Asano, S. Fujieda, S. Hashi, K. Ishiyama, T. Fukuda, and S. Suzuki, "Magnetic Domain Structure and Magnetostriction of Fe-Ga Single Crystal Grown by the Czochralski Method," *IEEE Magnetics Letters,* vol. 8, pp. 1-4, 2017.

[49] Y. He, J. M. D. Coey, R. Schaefer, and C. Jiang, "Determination of bulk domain structure and magnetization processes in bcc ferromagnetic alloys: Analysis of magnetostriction in Fe83Ga17," *Physical Review Materials,* vol. 2, no. 1, p. 014412, 2018.

[50] G. Raghunath and A. B. Flatau, "Study of magnetic domain evolution in an auxetic plane of Galfenol using Kerr microscopy," *Journal of Applied Physics,* vol. 117, no. 17, p. 17E704, 2015.

[51] G. Raghunath, M. Marana, S.-M. Na, and A. Flatau, "Kerr microscopy studies of the effects of bending stress on galfenol," *Journal of Applied Physics,* vol. 115, no. 17, p. 17E310, 2014.

[52] D. E. Parkes *et al.*, "Non-volatile voltage control of magnetization and magnetic domain walls in magnetostrictive epitaxial thin films," *Appl. Phys. Lett.,* vol. 101, no. 7, p. 072402, 2012.

[53] J. P. Joule, "XVII. On the effects of magnetism upon the dimensions of iron and steel bars," *The London, Edinburgh, and Dublin Philosophical Magazine and Journal of Science,* vol. 30, no. 199, pp. 76-87, 1847.

[54] H. D. Chopra, A. Ravishankar, M. S. Pacifico, and M. L. Forst, "Non-Joulian Magnetostriction and Non-Joulian Magnetism," *phys. stat. sol. (b),* vol. 0, no. 0, 2018.

[55] T. M. Saurav, M. L. Forst, J. A. Boligitz, and H. D. Chopra, "Contracting non-Joulian magnets," *Phys. Rev. B,* vol. 95, no. 17, p. 174425, 2017.

[56] V. Dabade, R. Venkatraman, and R. D. James, "Micromagnetics of Galfenol," *Journal of Nonlinear Science,* vol. 29, no. 2, pp. 415-460, 2018.

[57] Y. He, C. Jiang, J. M. D. Coey, and H. Xu, "Joulian magnetostriction of Galfenol Fe83Ga17," *Journal of Magnetism and Magnetic Materials,* vol. 466, pp. 351-353, 2018.

[58] B. D. Cullity and C. D. Graham, *Introduction to Magnetic Materials*, 2 ed. Hoboken, NJ: John Wiley and Sons, 2009.

[59] D. Chen, J. A. Brug, and R. B. Goldfarb, "Demagnetizing factors for cylinders," *IEEE Transactions on Magnetics,* vol. 27, no. 4, pp. 3601-3619, 1991.

[60] F. Bitter, "On Inhomogeneities in the Magnetization of Ferromagnetic Materials," *Physical Review,* vol. 38, no. 10, pp. 1903-1905, 1931.

[61] R. C. Hall, "Single Crystal Anisotropy and Magnetostriction Constants of Several Ferromagnetic Materials Including Alloys of NiFe, SiFe, AlFe, CoNi, and CoFe," *Journal of Applied Physics,* vol. 30, no. 6, pp. 816-819, 1959.

[62] R. Carey, "The Origin of the Band Structure Domain Pattern in Cube-textured Silicon-Iron," *Proceedings of the Physical Society,* vol. 80, no. 4, pp. 934-937, 1962.

[63] V. Stephan, "Zu den Bitterstreifenmustern auf Silizium-Eisen-Kristallen mit inneren Spannungen," *Experinmentelle Technik der Physik,* vol. 4, pp. 153-156, 1956.

[64] V. Stephan, "Magnetische Bereichsstrukteren in Silizium-Eisen-Kristallen mit inneren Spannungen," *Experinmentelle Technik der Physik,* vol. 5, pp. 145-162, 1957.

[65] W. D. Corner and J. J. Mason, "The effect of stress on the domain structure of Goss textured silicon-iron," *British Journal of Applied Physics,* vol. 15, no. 6, pp. 709-718, 1964.

[66] L. F. Bates and A. Hart, "Changes in Domain Structure accompanying Reduction in Depth of a Single Crystal of Silicon Iron," *Proceedings of the Physical Society. Section B,* vol. 69, no. 12, pp. 1200-1204, 1956.

A Standard Operating Procedure for Surface Preparation of Galfenol Single Crystals

This appendix will discuss the surface preparation process used in this work in the greatest detail possible, with consideration for sample cleanliness, polishing times, and some problems which may arise.

All polishing steps were performed on an Allied High Tech LaboPol-1 autopolisher. The full list of consumable materials used is as follows:

-PSA backed SiC paper discs, 600 and 800 grit (8 inch)
-Allied High Tech White Label Flexible Back Magnetic 8 inch disc
-Allied High Tech Imperial Flexible Back Magnetic 8 inch disc
-Buehler Microcloth Magnetic 8 inch disc
-Allied High Tech 1 μm Monocrystalline Diamond Compound
-Allied High Tech 0.04 μm Colloidal Silica Suspension
-Allied High Tech Red Lube
-Cotton balls
-Ethanol (190 proof)
-Nitrile gloves
-Dawn dish soap
-Clean paper towels

After acquiring the above materials, obey the following steps to achieve best results:

1. Use wet paper towels to wipe down all of the surfaces of the polishing head and polishing wheel to remove any leftover abrasive. Dry the wheel thoroughly before applying any polishing pads.
2. Apply a 600 grit SiC pad. With water running, polish at 15N of pressure until the epoxy is removed from the sample surface, 30-90 seconds.

3. Clean the sample with water and soap using a cotton ball to gently clean the surface. Spray the surface with ethanol and dry with a hair dryer. Place cotton balls in a small beaker and fill with ethanol. Place the sample face down on the cotton balls and place in ultrasonic cleaner for 1-2 minutes.
4. Repeat step 1.
5. Apply an 800 grit SiC pad. With water running, polish at 15N of pressure until the 600 grit scratches are removed, 2-6 minutes.
6. Repeat step 3.
7. Unscrew the bottom plate of the polishing head. Wash the plate thoroughly with soap and water. Clean the screws ultrasonically in the ethanol beaker for 1-2 minutes. At the same time, place the bottom plate of the polishing head in the water bath of the ultrasonic cleaner. Before reattaching the plate, thoroughly clean the rest of the polishing head with wet paper towels. Wear gloves while reassembling the autopolisher head.
8. Ensure that the polishing head is completely dry. While still wearing gloves, apply the Microcloth diamond pad. Place the sample on the pad to check for lubrication. If the pad is sufficiently lubricated, the sample surface should be wet with red lube. If the surface is too dry, apply Red Lube to the pad a few drops at a time until it is sufficiently lubricated.
9. Polish at 15N of pressure until the 800 grit scratches are removed and replaced with scratches which are thin and faint under 100X magnification, 3-6 minutes.
10. Repeat steps 3 and 7.
11. While still wearing gloves, apply the White Label pad. Without placing the sample on the pad, turn on the wheel and wet the pad thoroughly with colloidal silica. Polish at 15N of pressure until the largest scratches are removed, 4-6 minutes. Apply silica liberally while polishing, never allowing the pad to dry out. After removing the sample from the polisher, run water over the pad to prevent drying. There will still be some visible scratches.
12. Rinse the White Label pad thoroughly before storing.
13. Repeat steps 3 and 7.

14. While still wearing gloves, apply the Imperial pad. If the pad is dry, soak it with water before beginning. Periodically applying silica, polish at 15N of pressure until all scratches are gone, 5-50 minutes. Keep the pad from drying completely, applying a few drops of silica every 20-60 seconds. Listen for a knocking solid from the polishing head and adjust lubrication to minimize the sound. Whenever removing the sample for cleaning, immediately spray it with ethanol to cease any chemical reactions.
15. Repeat steps 3 and 1.

Some addition considerations should be taken during specific steps to maximize the effectiveness of the process.

During diamond polishing, the diamond paste can be washed from the pad very easily. Any water or lubricant that touches the pad will tend to remove abrasive. This pad should be lubricated very sparingly and only when necessary. This will reduce how often diamond paste must be reapplied

The White Label pad dries out more easily than the Imperial pad. It should be kept wet at all times to prevent drying of the silica. If silica dries onto the pad it can cake up and cause large scratches during polishing. This can also happen on the Imperial pad, but it dries more slowly so less care is required.

During the final stage in the process, when polishing on the Imperial pad, the scratches may become very small and shallow, making them difficult to see. To ensure that polishing is complete, ferrofluid must be applied to the sample. The ferrofluid tends to build up around invisible scratches to reveal them. Continue polishing until the surface quality is satisfactory even with the ferrofluid applied.

B Copyright documentation

Permission to use Figure 1.10 was granted through the Copyright Clearance Center, Order License Id 4632530166852

Permission to use Figure 1.15 and Figure 1.16 was granted through the Copyright Clearance Center, Order License Id 4632530167979